Revisiting crop water stress index based on potato field experiments in Northern Germany

Elmer Kanjo Ekinzog [a], Martin Schlerf [a,*], Martin Kraft [b], Florian Werner [c], Angela Riedel [d], Gilles Rock [e], Kaniska Mallick [a]

[a] Luxembourg Institute of Science and Technology, ERIN Department, Remote Sensing and Natural Resources Modelling Group, 41 rue du Brill, L-4422 Belvaux, Luxembourg
[b] Federal Research Institute for Rural Areas, Forestry and Fisheries, Thünen Institute of Agricultural Technology, Bundesallee 47, 38116 Braunschweig, Germany
[c] Hydrosat S.à. r.l., 9 rue du Laboratoire, L-1911, Luxembourg
[d] Agricultural Chamber of Lower Saxony, Fachbereich Pflanzenbau, Wunstorfer Landstraße 9, 30453 Hannover, Germany
[e] Luxsense Geodata, 4, rue Albert Simon, L-5315 Contern, Luxembourg

ARTICLE INFO

ABSTRACT

Different types of the Crop Water Stress Index (CWSI) have been useful for water stress monitoring and irrigation management in semi-arid regions, however little research exists on its effective application in humid regions. This study aims to assess the effectiveness of three CWSI models (CWSIe - empirical, CWSIt - theoretical, CWSIh - hybrid) for crop water stress monitoring in an experimental field for potato crops in Northern Germany. Irrigation experiments with three treatments (optimum-OP, reduced-RD and no) were conducted in the summer of 2018 and 2019. Continuous canopy temperatures (Tc) for OP and RD irrigation treatments together with meteorological measurements were used to derive CWSI from the different models. Additionally, Visible/near infrared (VNIR) and Thermal Infrared (TIR) drone images were collected on several days during the growing season to create CWSI maps. The different CWSI models were correlated with volumetric soil water content (θ) measurements for comparison and relationships were established between CWSI and θ for prediction. Results showed that CWSI accurately estimates soil water content under atmospheric conditions similar to those in semi-arid regions. The predictive performance of different CWSI models were fairly good ($R^2 = 0.57$–0.63) (situation in 2019). CWSIe and CWSIh performed better than CWSIt. CWSI-θ relations calibrated in one year effectively predicted θ in another year with errors of 1.2–2.2% absolute soil water content. CWSIh could be a promising alternative to the traditional CWSI as it combines aspects of CWSIe (empirical upper limit) and of CWSIt (theoretical lower limit) which has advantages for operational use. Finally, the drone-based CWSI and θ maps (derived from the developed CWSI- θ relations) captured well the applied irrigation patterns and could help to decide when to irrigate and how much water to apply.

1. Introduction

Irrigation is the biggest user of freshwater on Earth; however, a large proportion of irrigation water is wasted due to inefficient irrigation systems (Cohen et al., 2017). Water supply for irrigation is expected to decrease due to frequent droughts and increased competition from other industries around the world (Alvino and Marino, 2017). Hence, there is a need for improved irrigation management to optimize irrigation water use while maximizing crop yield (Rud et al., 2014; Cohen et al., 2017; Han et al., 2018). Crop water status is an important water stress indicator used in irrigation management (Cohen et al., 2017; Han et al.,

2018). Although soil-based methods for assessing crop water status are more widely used, there is a growing interest in plant-based methods (Jones and Vaughan, 2010), because they serve as a direct proxy of actual plant water status, whereas soil water content measurements only provide an indirect linkage. Canopy temperature (Tc) is a good indicator for water status due to its inverse relation to the rate of canopy water loss which in turn is closely linked to stomatal conductance (Jones and Vaughan, 2010), hence Thermal Infrared (TIR) sensing of Tc has been a useful tool for monitoring water stress (Alvino and Marino, 2017; Han et al., 2018; Bian et al., 2019). However, the sensitivity of Tc to changing weather conditions led to the development of crop water stress index

(CWSI) which considers the effects of air temperature (Ta) and other meteorological variables such as vapor pressure deficit (VPD), wind speed (WS) and available energy.

The Crop Water Stress Index (CWSI) has been proven to be effective in water stress monitoring and in irrigation management (DeJonge et al., 2015; Alvino and Marino, 2017). Its main advantage over pure Tc measurements is that it accounts for meteorological variables, mainly, Ta and VPD, while Tc alone is sensitive to highly fluctuating environmental factors (Inoue et al., 1990), which makes CWSI a more suitable measure of water stress. CWSI is based on a solid theoretical base (Idso et al., 1981) and it normalises Tc firstly, by the actual difference between canopy and air temperature (known as canopy-to-air temperature difference, Tc-Ta or CATD) and secondly, by the Tc-Ta of fully transpiring and non-transpiring crops commonly referred to as the lower and upper limits respectively (Jackson et al., 1981). Different models to calculate CWSI have been developed based on differences in how the upper and lower limits are derived (Maes and Steppe, 2012). The Empirical CWSI – CWSIe (Idso et al., 1981) model establishes a relationship between Tc-Ta and VPD from which the lower limit, known as the "non-water-stressed baseline" – NWSB (Idso et al., 1981), is derived. The main advantage of CWSIe is that it requires the measurement of only three variables (Tc, Ta, and VPD) for its application. However, the NWSB is highly sensitive to changes of climate variables, such as radiation and wind speed (Jackson et al., 1988; Gonzalez-Dugo et al., 2014). Yearly differences in NWSBs have also been reported for the same crop in the same field (Horst et al., 1989; Gonzalez-Dugo et al., 2014; Han et al., 2018), hence the use of baselines derived from one year across multiple years has been questioned. Additionally, a robust NWSB is usually derived at the end of the growing season from multiple cloud free days (Gardner et al., 1992a, 1992b), which makes the near-real time application of CWSI challenging for day-to-day stress measurements during the growing season.

The theoretical CWSI - CWSIt (Jackson et al., 1981) model presents an alternative method for calculating the upper and lower limits from equations based on a combination of the Penman-Monteith and the energy balance equation. It offers an improvement to CWSIe by including additional atmospheric parameters, net radiation (Rn), wind speed (WS), and canopy resistance (r_C) which are not considered in the CWSIe (Jackson et al., 1981, 1988). CWSIt in principle is advantageous over CWSIe for practical use in day-to-day water stress monitoring since its upper and lower limits are derived from equations applied for the same environmental conditions at the time of Tc measurement (Jackson et al., 1988). Nevertheless, CWSIt has a number of disadvantages: Firstly, problems attributed to the proper estimation of aerodynamic resistance (r_A) from wind speed were noted by Jackson et al. (1988) and has been shown to significantly affect final CWSIt values (Stockle and Dugas, 1992; Agam et al., 2013b). Secondly, net radiation (Rn) is another important input variable required, however, which is not directly measured in many weather stations and therefore needs to be estimated from meteorological variables (Berni et al., 2009). Accurate estimation of aerodynamic resistance, r_A, poses challenges as estimates depend on the empirical parameterization of surface roughness and atmospheric stability corrections which further requires a number of site-specific parameters (Paul et al., 2014; Mallick et al., 2016, 2018) and has led to errors in the final CWSI estimates (Berni et al., 2009). Given the limitations associated with deriving r_A, a method that eliminates the need for estimating r_A could improve the accuracy of CWSI. Rud et al. (2014) demonstrated that the use of empirical upper limits together with theoretical lower limits did not affect the accuracy of final CWSI values and Agam et al. (2013a) recommended its use for practical purposes. The use of empirical upper and theoretical lower limits to calculate CWSI is further investigated and is referred to as hybrid CWSI model (CWSIh) henceforth.

The development and early application of CWSI was done on point-based Tc measurements, but has been adapted and applied to high resolution thermal imagery for assessing the spatial variability of crop water status (Jones, 1992; Maes and Steppe, 2012; Agam et al., 2013b).

Direct/image-based models involving different ways of deriving the upper and lower limits (Jones, 1992, 1999; Fuentes et al., 2012; Padhi et al., 2012; Gerhards et al., 2018); theoretical models with direct application of theoretical equations from Jackson et al. (1988); and hybrid models with a fixed upper limit (depending on crop type) and theoretical lower limit, have widely been applied to TIR images (Jones, 1999, 1992; Möller et al., 2006; Rud et al., 2014; Hoffmann et al., 2016).

The applicability of CWSI for water stress monitoring depends on demonstrating that it can accurately and reliably replace soil and plant-based water status indicators in agricultural fields and that it is appropriate for stress detection in a variety of crops in different climatic zones (Cohen et al., 2017). Suitable relationships between CWSI and other indicators are required in order to translate CWSI accurately into water-stress estimates, which can then serve in irrigation decision support (Möller et al., 2006). CWSI has been shown to exhibit good relationships with direct in situ plant and soil-based measures such as soil water content (Padhi et al., 2012; DeJonge et al., 2015; Taghvaeian et al., 2014), leaf water potential, stomatal conductance and transpiration (Berni et al., 2009; Gonzalez-Dugo et al., 2013; Cohen et al., 2017; Han et al., 2018; Bian et al., 2019). In this study, relationships between volumetric soil water content (θ) and thermal stress indices are explored and used to evaluate the performance of indices in monitoring water stress. Such relationships normally derived from point measurements are potentially transferable to images to represent stress at large spatial scales (Berni et al., 2009; Gonzalez-Dugo et al., 2014; Rud et al., 2014). Here, established relationships between CWSI and soil water content are transferred to drone images and their accuracy was evaluated to represent the spatial variability of soil water content.

CWSI was developed to provide a universal method of water stress monitoring for agricultural crops in different climatic zones (Jackson et al., 1988) and so far, has been proven to be robust in many arid and semi-arid regions around the globe and for different agricultural crops (Meron et al., 2013; DeJonge et al., 2015; Cohen et al., 2017; Liu et al., 2020;). However, little research has been carried out so far to test its applicability in humid and sub humid regions, including possible linkages of CWSI with soil water content, although vegetation in these regions is also susceptible to water stress. In order to be considered a truly universal approach, it's robustness must be tested across a broad range of climatic and aridity zones. Jones (1999) investigated the potential use of infrared thermometry in cooler humid climates and Hoffmann et al. (2016) in their studies in western Denmark proved that CWSI could accurately represent the water status of barley. In the present study, we test the suitability of CWSI in potatoes as a tool for irrigation support in a temperate humid zone of Northern Germany.

The objectives of this study were to:

- Derive and assess the performance of three CWSI models (CWSIe, CWSIt, CWSIh) as a proxy for crop water stress through relations with volumetric soil water content (θ).
- Assess the transferability of derived CWSI-θ relations from one year to another year and its applicability to drone-based CWSI images for mapping soil water content at field scale.
- Discuss the suitability of Crop Water Stress Index as a water stress indicator in a humid region on potato, a crop susceptible to water stress.

2. Materials and Methods

2.1. Description of experimental setup and design

The experiment was carried out in Hamerstorf in Northern Germany (52° 54' 36'' N, 10° 27' 36'' E; 65 m a.s.l.), a site with annual rain totals of 622 mm and mean annual air temperature of 8.8 °C and with silty sand being the primary soil type. The experimental site belongs to the Agricultural Chamber of Lower Saxony (Landwirtschaftskammer Niedersachsen, LWK), which has been conducting irrigation experiments

for more than 13 years with the main objective to assess the effect of irrigation intensities, representing different levels of water stress, on crop yield. The experimental data has been collected within the project "Sensor based irrigation control in potatoes" which ran from 2016 to 2019 with the main aim to "use canopy temperature for irrigation decision support and how the techniques can be implemented into agricultural operating systems (Meinardi et al., 2021).

This study investigates the effect of different irrigation water treatments on potato crops carried out over two years 2018 and 2019. The variety in each year was "Amanda". The root depth has not been measured, but the assumption was, that the maximum root depth of the potato plant is 60 cm. Former measurements of soil water content at different depths showed water extraction by the root at a maximal depth of 60 cm. The potato crops were planted on a 270 m x 42 m field divided into 120 plots (representing 2 different irrigation treatments, 2 different potash fertilization regimes, 4 repetitions of each treatment, and 2 auxiliary plots for each of the 40 experimental plots) of 9 m x 6,75 m, with a planting density of 4 plants per square meter on 9 rows of ridges in each plot. Each plot had a total length of 27 m, where only the 9 m in the middle are harvested (net harvest plot), Three different types of irrigation treatments were implemented based on the desired percent of usable field capacity (nFK, Table 1), developed based on experiences from long-term irrigation experiments carried out by LWK. Optimum irrigation (OP hereafter) with 50% nFK (also referred to as CWSI 0.5) means a good water supply for the plants with no relevant drought stress, aiming at highest possible yield; Reduced irrigation (RD hereafter) with 35% nFK (also referred to as CWSI 0.65) means temporary drought stress with possible effects on yield, aiming at a reduced water and energy consumption, and no irrigation as control treatment. The control treatment will not be regarded for CWSI measurement in this paper.

A nozzle cart with a boom, made by Beinlich (Ulmen, Germany)[1], was used for irrigation. The adjustment of the retraction velocity of the cart was made based on water pressure, water amount per hour and nozzle width. The true amount of water was controlled with 4 customary plastic rain gauges along the irrigation width. The deviation of the given amount was approx. $\pm$ 2 mm. The decision on when and amount to irrigate was based on weekly/bi-weekly gravimetric soil water content (θ_g) measurements in combination with transpiration amounts for the following days according to the weather forecast from DWD (German weather Service) (water-balance method according to Hartmann et al., 2000). The root zone was considered as 60 cm depth from top of dam (45 cm below planting depth) at development stadium BBCH 55 (first bud 5 mm).

Final irrigation dates and amounts are presented in Table 2. Irrigation treatments started on 42 days after planting for OP plots and 45 days for RD plots in 2018 and 52 days after planting for OP plots and 69 days for RD plots in 2019, both set approximately at the beginning of inflorescence emergence and tuber formation in 2018 and 2019 respectively, because these are the periods when water consumption by potato is highest (Dalla Costa et al., 1997; Gerhards et al., 2016) with the exception of OP in 2019, when irrigation started at the beginning of tuber initiation for quality reasons.

2.2. Canopy temperature, soil water content and meteorological measurements

Six thermal infrared thermometers (IRT), Thünen Institute in-house development and construction based on the Sensor Chip Melexis MLX90614, with massive aluminium housing, special electronics for MODBUS protocol usage and additional radiation shielding were set up at six plots to record continuous canopy temperatures (Tc) of three RD (CWSI 0.65) and three OP (CWSI 0.5) replications from June to

Table 1
Table of abbreviations, constants, symbols, and their description used in the study.

Symbol	Description
TIR	Thermal Infrared
CWSI	Crop Water Stress Index
CWSIe	Empirical Crop Water Stress Index
CWSIt	Theoretical Crop Water Stress Index
CWSIh	Hybrid Crop Water Stress Index
DN	Digital numbers
BT	Brightness temperature (°C)
OP	Optimum irrigation
RD	Reduced irrigation
nFK	Usable field capacity, also called available water capacity nFK=FC-PWP
PWP	Permanent wilting point
FC	Field capacity
Ta	Air Temperature (°C)
VDP	Atmospheric vapor pressure deficit (hPa) at the level of Ta measurement
e_a^*	Saturation vapor pressure of surface (hPa) at Ta
e_a	Actual vapor pressure at air temperature (hPa)
VPG	Vapor pressure gradient (hPa)
Tc-Ta/ CATD	Canopy-to-air temperature difference (°C)
θ	Volumetric soil water content ($m^3\ m^{-3}$)
Rn	Net radiation ($W\ m^{-2}$)
WS	wind speed
r_C	canopy resistance ($s\ m^{-1}$)
r_{CP}	canopy resistance at full transpiration ($s\ m^{-1}$)
r_A	aerodynamic resistance ($s\ m^{-1}$)
G	Ground heat flux ($W\ m^{-2}$)
Rg	Incoming Shortwave radiation ($W\ m^{-2}$)
Rso	clear-sky solar radiation ($W\ m^{-2}$)
RH	Relative humidity (%)
ρ	Density of air ($kg\ m^{-3}$)
c_P	Specific heat of dry air ($J\ kg^{-1}\ °C^{-1}$)
Δ	Slope of saturation vapor pressure versus temperature curve (hPa $°C^{-1}$)
γ	Psychrometric constant (hPa $°C^{-1}$)
z	reference height (m)
d	displacement height (m)
z_0	roughness length (m)
$(Tc-Ta)_{UL}$	upper reference under non-transpiring conditions (°C)
$(Tc-Ta)_{LL}$	lower boundary representing a non-water-stressed condition (°C)
NWSB	Non water stressed baseline equivalent to $(Tc-Ta)_{LL}$
Twet	lower boundary of plant/canopy surface temperature (°C)
Tdry	upper boundary of plant/canopy surface temperature (°C)
α	Soil surface albedo
σ	Stefan Boltzmann constant
Rg_{clr}	Clear sky radiation ($W\ m^{-2}$)
GR_{coef}	Coefficient representing G/RN

September for each year. Tc was recorded every 3 seconds and averaged over 30 minutes. Only Tc data in the timespan from 11 am to 3 pm Central European Summer Time (CEST) were used in this study, unless indicated else. This is 9:38 am to 1:38 pm local solar time. The mean of the three OP or RD replications were used for stress analysis. The IRTs had a thermal resolution of 0.02 K. Their field of view angle was 35°. To ensure that only pure Tc was monitored even before full canopy closure, IRTs were installed at an oblique angle of 60° to nadir, so that their field of view captured only vegetation. IRTs were mounted at 2 m above ground, resulting in an elliptical measurement area of about 5 m^2 per sensor at ground level. IRTs were positioned at the Northern border of each plot, pointing towards South. The emissivity was set to 1, despite the fact that real dense crop canopies have slightly lower emissivity, and background (sky) radiation should be taken into account for precise IRT measurements. No canopy temperature was measured in the non-irrigated plots. From previous experiments it was known that non-irrigated potato plants almost never arrive at full canopy cover on the sandy soil, thus prohibiting any valid canopy temperature measurement by IRTs. Growing potatoes without irrigation does not occur on real production fields in the local irrigation region.

Table 2

Planting and harvesting date, irrigation amounts (in mm) for each treatment and crop growth stages as BBCH (FAO-56) for each treatment. Values in parenthesis indicate the number of irrigation events. Irrigation was the same for treatments OP (50% nFK and 0.5 CWSI) and RD (35% nFK and 0.65 CWSI), on all dates except in the period 22–29 July 2019.

2018					2019				
Date	OP 50% nFK	RD 35% nFK	BBCH	Growth Stage	Date	OP 50% nFK / 0.5 CWSI	RD 35% nFK / 0.65 CWSI	BBCH	Growth Stage
27-Apr	Planting				15-Apr	Planting			
08-Jun	25		55	Inflorescence emergence (crop development)	04-Jun	20		40/19	Beginning of Tuber formation/end of leaf development (crop development)
11-Jun		25	55						
14-Jun	28								
18-Jun		29	60	Flowering (mid-season 1)	21-Jun	25	25	61	Flowering (mid-season)
27-Jun	30		66		27-Jun	30		65	
02-Jul		30	69		01-Jul		30	69	
04-Jul	30				03-Jul	30		69	
09-Jul	25	25	72	Tuber Development (mid-season 2)	18-Jul	25		75	Tuber Development (mid-season)
19-Jul	30		74		22-Jul		25/		
23-Jul		30	75		25-Jul	30/			
26-Jul	30		76		26-Jul		/ 30	91	Senescence (late season)
30-Jul		31	78		29-Jul	/ 30		91	
02-Aug	30		91	Senescence (late season)					
07-Aug	25		91						
25-Sep	Harvest				16-Sep	Harvest			
Sum	**253 (9)***	**170 (6)***			**Sum:**	**160 (7)***	**85 (4)***		

*Numbers in brackets represent number of irrigation events in the season

Continuous volumetric soil water content (θ) measurements were made with two Sentek EnviroScan sensors (Sentek Sensor Technologies, Australia) at positions IR1 and IR2 (Fig. 1) to represent soil moisture conditions for RD and OP respectively. Both EnviroScan sensor tubes contained 6 sensors and were placed covering the top 60 cm soil profile in intervals of 10 cm. θ measurements for 2018 and 2019 were carried
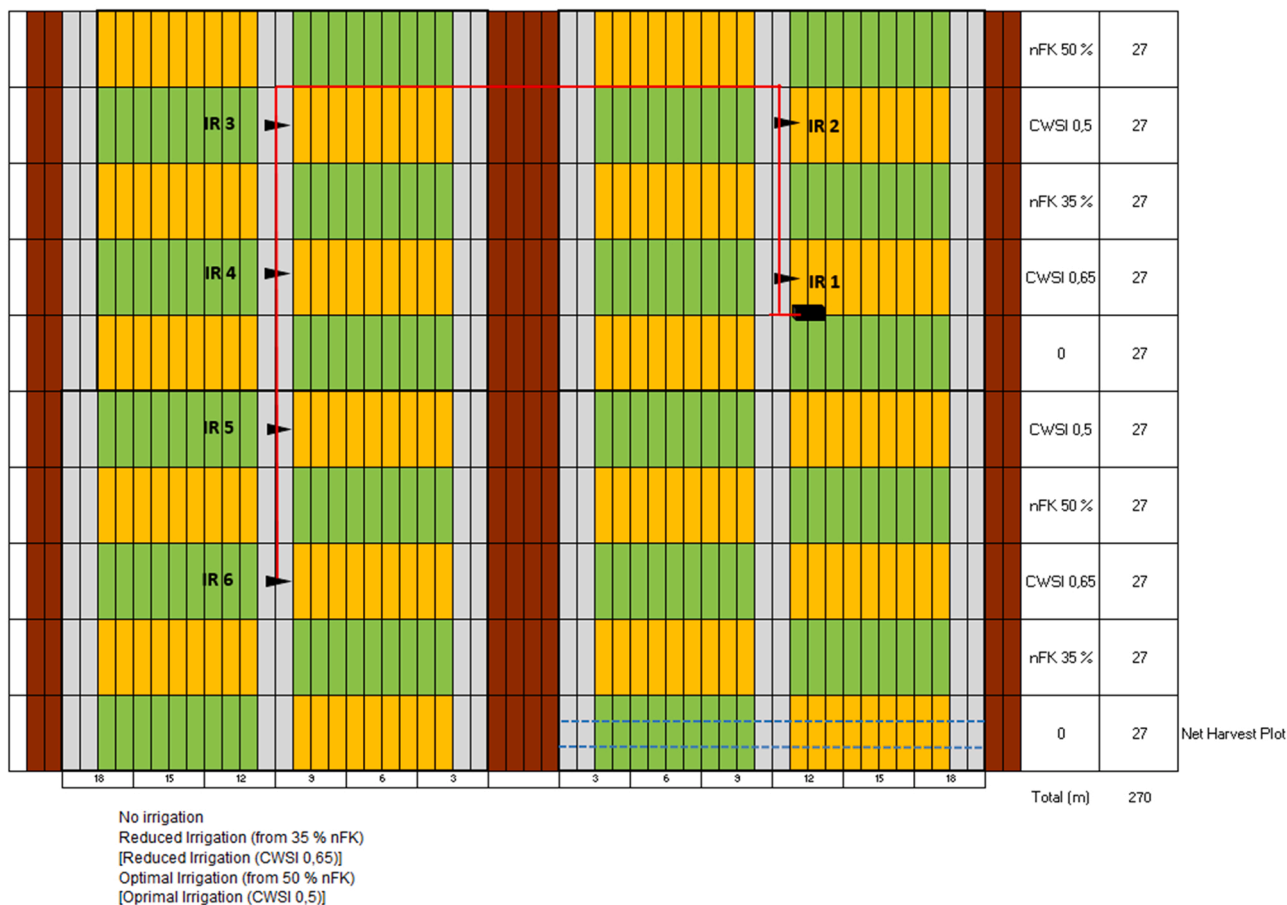

Fig. 1. Setup of irrigation experiment, IR 1–6 are the approximate positions and direction of view of thermal infrared thermometers (IRT) and the corresponding irrigation treatments applied to each field portion in 2019. Colors green and orange denote two different potash fertilization treatments which are not considered in this study. Fertilization was done according to common local agricultural practice for the plots used for IRT measurement.

Table 3

Summary of meteorological measurements for June, July, August for the 2018, 2019 growing seasons.

Parameter	Jun - Aug 2018	Jun - Aug 2019
Global Radiation$_{mean}$ (Wm-2)	323	315
Air Temp$_{mean}$ (°C)	19.0	18.9
Air Temp$_{max}$ (°C)	36.7	37.0
Air Temp$_{min}$ (°C)	6.1	5.0
Relative Humidity$_{max}$ (%)	99.6	100.0
Relative Humidity$_{min}$ (%)	20.8	21.3
Wind Speed (ms-1)	1.7	1.5
Rain$_{sum}$ (mm)	91	165

out at two different locations. In 2018 the soil moisture sensors were placed in the valley between two ridges and in 2019, soil moisture measurements were done at the top of the ridge where the potato plant grows. Additionally, gravimetric water content (θg) measurements for the top (0–30 cm), bottom (30–60 cm), and full (0–60 cm) soil profile were made following a standard protocol (Wessolek et al., 2009) approximately every 1–2 weeks at 2 locations each representing an OP or RD treatment. 3 samples were taken per plot, followed by mixing and scaling the samples before putting them into a drying oven for approximately 20 hrs at 105 °C, then scaling the samples again. Soil density, field capacity (15–18% volume for 0–30 cm depth; 11–14% for 30–60 cm depth) and permanent wilting point (approx. 3–4 Vol%) were estimated based on soil texture (Wessolek et al., 2009). Soil texture varied between the plots. It was estimated for each sample separately by hand (finger test). The highest FC and PWP values occurred in the upper soil (0–30 cm) due to the higher soil organic carbon content (1.5%).

Meteorological measurements of air temperature (Ta), solar radiation (Rg), relative humidity (RH), and wind speed (WS), were measured every 2 minutes at position IR1 in the field (Fig. 1). Daily rainfall was recorded at a weather station located on the experimental site. Additional meteorological parameters such as vapor pressure deficit (VPD) and net radiation (Rn) were calculated according to (Allen et al., 1998, 1994a, 1994b) and ground heat flux (Gn) was estimated for wet soils according to Santanello and Friedl (2003). Summary of meteorological conditions for the two years of the experiment are shown in Table 3.

2.3. Unmanned aerial system (UAS) image acquisition and processing

Visible/near infrared (VNIR) and Thermal Infrared (TIR) images over the plot data were collected on four days in the growing season of 2019 (19 June at 13:45, 26 June at 15:15, 24 July 14:10 and 24 August at 10:30, 12:00, 13:50 and 15:20). Each flight lasted for approximately 20–30 minutes along 8 flight lines per field. The flight lines were programmed to have 70% side overlap and flight altitude was set to 60 m above ground. Image GPS positions were recorded for every flight.

Visible/near infrared (VNIR) were collected with the MicaSense RedEdge-MX™ sensor (MicaSense, Inc., Seattle, WA, USA) multispectral camera with five spectral bands (i.e., blue, green, red, red-edge and near infrared (NIR). Details on different bands, wavelengths and bandwidths are shown in Table 4. The camera setup includes a GPS module which allows geotagging every single image collected. A downwelling Light

Table 4

Sensors used and their properties.

Sensor	Parameter	Value
MicaSense RedEdge-MX™	Resolution	5 cm
	Blue band	475 nm (20 nm bandwidth)
	Green band	560 nm (20 nm bandwidth)
	Red band	668 nm (10 nm bandwidth)
	Red Edge band	717 nm (10 nm bandwidth)
	NIR band	840 nm (40 nm bandwidth)
TeAx ThermalCapture Fusion Zoom	Resolution	5 cm
	Thermal IR band	10500 nm (6000 nm bandwidth)

Sensor (DLS) in the camera monitors varying illumination conditions during light overcast. A reflectance calibration target with a set of 5 panels coated with differing grey intensities and whose reflectance spectra had been measured in a laboratory was installed next to the fields and was used for image calibration and correction. Downwelling radiation measured with the DLS were used to correct for varying illumination conditions in every single frame. The raw DN images then underwent photogrammetric processing in Agisoft Metashape resulting in georeferenced orthomosaic images. A step- and band wise empirical line correction was used to convert DN to surface reflectance values. Linear relationships fitted between image DN and surface reflectance values from the calibration panels were used to develop prediction equations (with R^2 values greater than 0.9) for surface reflectance calibration for each date and band.

Thermal infrared (TIR) images were captured using the Thermal-Capture Fusion Zoom camera (https://thermalcapture.com/thermalcapture-fusion-zoom-50mm/). The camera contains a thermal FLIR Tau 2 core with a thermal resolution of 0.05 K and records GPS positions. Image data with a spatial resolution of 640×512 pixels was collected with 9 Hz frequency. Conversion of digital numbers (DN) to brightness temperature (BT) was carried out in TeAx Thermoviewer using an assumed emissivity of 1. Raw images were selected to have 80% front overlap and were subjected to a photogrammetric processing workflow using Agisoft Metashape. Canopy temperatures (Tc) were retrieved from BT according to the two-step process described in Heinemann et al. (2020). First land surface emissivity (LSE) maps were derived from NDVI and then the derived LSE used to calculate Tc. Accuracy of the retrieved Tc from the drone data, was verified against ground thermometers at positions of IRT sensors (IR 1 - 6; Fig. 1), after extraction of "pure" image Tc using NDVI masking (Zhang et al., 2019). Results gave an R^2 value of 0.71 and RMSE of 2.1 °C.

2.4. Crop water stress index (CWSI)

CWSI (Idso et al., 1981; Jackson et al., 1981) was defined according to:

$$CWSI = \frac{(Tc-Ta) - (Tc-Ta)_{LL}}{(Tc-Ta)_{UL} - (Tc-Ta)_{LL}} \quad (1)$$

where (Tc-Ta) is the measured temperature difference between canopy and air in °C, (Tc-Ta)$_{LL}$ is the lower boundary representing a non-water-stressed condition. (Tc-Ta)$_{UL}$ is the upper reference under non-transpiring conditions. For a well-watered crop, CWSI value is close to 0; whereas for the crop under severe water stress condition, CWSI value is close to 1. Several different models for CWSI estimation have been developed based on the different methods of calculating the (Tc-Ta)$_{LL}$ and (Tc-Ta)$_{UL}$ (Han et al., 2018).

2.4.1. Empirical CWSI (CWSIe)

According to the empirical model in Idso et al. (1981), Tc -Ta follows a linear relationship with VPD (Fig. 2). When crops are sufficiently well-irrigated, a regression line, the so-called non-water-stressed baseline (NWSB), which is equivalent to (Tc -Ta)$_{LL}$, can be derived according to Eq. 2 as:

$$(Tc-Ta)_{LL} = aVPD + b \quad (2)$$

where: coefficients a and b are determined by linear regression of the scatterplot between (Tc - Ta) versus VPD and (Tc -Ta)$_{LL}$ is the NWSB.

To achieve the linear relationship represented in (Fig. 2), to be applied in Eq. 2 two methods have typically been established (Gardner et al., 1992a, 1992b) and were used in this study.

a. *Single-day method*, where diurnal measurements from a well-watered crop are taken throughout a day to capture a wide range of Tc - Ta and VPD values. A plot of Tc - Ta vs VPD is done and a negative linear
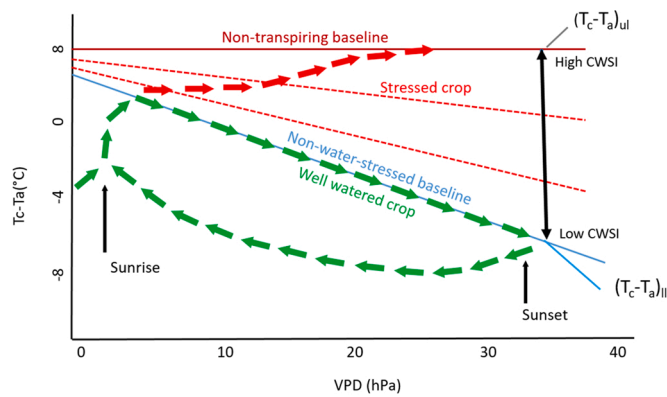
Fig. 2. Schematic illustration of the empirical CWSI. The red arrow shows the evolution of the canopy-air temperature difference (Tc-Ta) of a stressed crop over a day. The green arrows show the change of Tc-Ta of a well irrigated crop over a day. The linear blue line is the non-water stressed baseline. Red dashed lines are isolines indicating the same level of water stress (Modified after Idso et al., 1981 and Deng, 2015).

regression line can be fitted from the period sometime after sunrise and sunset as shown in Fig. 2 (Idso et al., 1981; Gardner et al., 1992a, 1992b). To establish the $(Tc - Ta)_{LL}$ using the empirical single-day method in this study, days with sufficient difference between OP and RD treatments (established through soil water content differences) were selected. The relationships between Tc - Ta against VPD throughout the day was examined and days in which suitable negative linear relationships could be established after sunrise and before sunset as demonstrated in Fig. 2 were used to obtain parameters for the NWSB and Eq. 2. Maximum Tc - Ta from stressed crops were used for $(Tc - Ta)_{UL}$.

b. *Multi-day method*, in which measurements can be made for well-watered crops on several days in a growing season, usually at the exact same time 1–2 hours around solar noon when VPD is maximum when water stress is likely to be the highest (Gardner et al., 1992a, 1992b; Irmak et al., 2000).

To establish the $(Tc - Ta)_{LL}$ with the multi-day method, Tc and VPD measurements were selected on several cloud free days from OP treatments, 1 and 2 days after irrigation and significant rain event (> 11 mm) between 11 and 15 h CEST (Idso et al., 1981; Han et al., 2018). Parameters for the NWSB were generated from the negative linear relationship established between Tc – Ta and VPD. Cloud free days were considered to be days where the ratio of incoming solar radiation to clear-sky solar radiation (Rso) was greater than 0.7 (Taghvaeian et al., 2012). $(Tc-Ta)_{UL}$ was calculated according to Eq. 3.

The Non-transpiring baseline (NTB, Fig. 2) can be based on maximum Tc measurements of an extremely stressed crop or - equivalent to determination of the NWSB - based on Eq. 3 (Han et al., 2018):

$$(Tc- Ta)_{UL} = aVPG + b \tag{3}$$

where: a and b are the slope and intercepts derived from Eq. 2 and VPG is vapor pressure gradient defined as the difference between the saturation vapor pressure evaluated at air temperature (Ta) and at a higher air temperature equal to air temperature plus "b", Ta + b, as shown in Eq. 4 (Allen et al., 1998; Han et al., 2018):

$$VPG = 6.1e^{\left(17.27\frac{Ta + b}{(Ta + b) + 237.3}\right)} - 6.1e^{\left(17.27\frac{Ta}{Ta + 237.3}\right)} \tag{4}$$

2.4.2. Theoretical CWSI (CWSIt)

Theoretical CWSI is based on equations derived from the combination of Penman-Monteith equation and the energy balance equation (Jackson et al., 1981):

$$(Tc- Ta) = \frac{r_A(Rn- G)}{\rho c_P} \times \frac{\gamma\left(1 + \frac{r_C}{r_A}\right)}{\Delta + \gamma\left(1 + \frac{r_C}{r_A}\right)} - \frac{VPD}{\Delta + \gamma\left(1 + \frac{r_C}{r_A}\right)} \tag{5}$$

where, c_P is the heat capacity of air (J kg^{-1} °C), VPD is the air vapour pressure (Pa), γ is the psychrometric constant (Pa ° C^{-1}), r_A is the aerodynamic resistance (s m^{-1}), r_C is the canopy resistance (s m^{-1}), Δ is the change (slope) of saturation vapour pressure with temperature (Pa ° C^{-1}), Rn is the net radiation (J m^{-2} s^{-1}), G is heat flux consumed by soil (J m^{-2} s^{-1}).

The aerodynamic resistance r_A can be expressed as:

$$r_A = \frac{4.72[ln(z - d)/z_0]^2}{1 + 0.54WS} \tag{6}$$

where z is the reference height (m), d is the displacement height (m), d = 0.63 *h, h is the height of crop (m), z_0 is the roughness length (m), z_0 = 0.13 *h, and WS is the wind speed at height z (m^2 s^{-1}) (Jackson et al., 1981).

The $(Tc -Ta)_{UL}$ is derived by assuming an infinitely large canopy resistance ($r_C \approx \infty$), reducing Eq. 5 to Eq. 7:

$$(Tc- Ta)_{UL} = \frac{r_A(Rn- G)}{\rho c_P} \tag{7}$$

$(Tc -Ta)_{LL}$ is modelled for conditions when $r_C = r_{CP}$ (the canopy resistance at full transpiration). According to Jackson et al., (1988, 1981), r_{CP} can be assigned a value of zero or a known r_{CP} value. In this study, $r_{CP} = 0$ was used reducing Eq. 5 to Eq. 8:

$$(Tc- Ta)_{LL} = \frac{r_A(Rn- G)}{\rho c_P} \times \frac{\gamma}{\Delta + \gamma} - \frac{VPD}{\Delta + \gamma} \tag{8}$$

2.4.3. Hybrid CWSI (CWSIh)

Both empirical and theoretical CWSI models show clear drawbacks: empirical approaches require suitable environmental conditions, and theoretical models require estimates of resistance terms and accurate net radiation calculations. The non-transpiring baseline $(Tc - Ta)_{UL}$ shows a weaker dependence on environmental conditions, e.g., VPD, compared to the non-water-stressed baseline $(Tc – Ta)_{LL}$. It is also challenging to observe fully transpiring vegetation under high evaporative demand (high Rn and VPD), as also well-watered vegetation can show reduced transpiration under such conditions. Accordingly, determination of the non-transpiring baseline in the empirical method is more consistent between years and relies less on identifying suitable days (see Section 3), if at least some dry periods are observed during the growing season.

We propose using an empirical estimate of the non-transpiring baseline to calculate the non-water-stressed baseline from a theorical model. Substituting Eq. 7 in Eq. 8 shows that with a known $(Tc - Ta)_{UL}$, the $(Tc – Ta)_{LL}$ can be derived without the need to estimate r_A, Rn and G leading to a simplification:

$$(Tc- Ta)_{LL} = (Tc- Ta)_{UL} \times \frac{\gamma}{\Delta + \gamma} - \frac{VPD}{\Delta + \gamma} \tag{9}$$

For the hybrid method, a fixed upper baseline developed from the empirical method was used.

2.4.4. Statistical analysis

Canopy temperature and meteorological variables can change quickly within a few seconds; hence all measured values were averaged over 30 min to level out short-term fluctuations. For example, values at solar noon 13:19 CEST in this analysis is the average of measured data from 13:04–13:34 CEST. Days on which irrigation was done or the total rain was > 1.0 mm were not included, since the wet surface of the leaves can falsify the temperature measurement.

For all analysis, CWSI values for the three indices (CWSIe, CWSIt, CWSIh) were calculated for each IR (1−6) sensor and averaged only

after calculation. Plots and analysis are presented only for full cover periods (20 June - 08 August 2018 and 19 June - 06 August 2019), since it can be largely ensured during this period that little, or no soil was visible in the measuring range of the sensor. Other researchers applied similar restrictions, e.g. when canopy cover was larger than 70% (DeJonge et al., 2015) or when crop coverage in the field of view of IRTs was larger than 80% (Han et al., 2018).

Pearson correlation coefficients (*r*) between midday (11:00–15:00 h CEST) CWSI and measured soil water content (θ) at 10 cm depth was used to evaluate the suitability of the indices in monitoring water stress. Since θ measurements were taken only at positions IR1 and IR2 representing one RD and OP treatments respectively, only Tc and the three CWSI models developed for these 2 treatments were used to establish relationships with θ. To predict θ from CWSI, exponential relationships were established for CWSI and θ for one year and used to predict θ for the other year and for Tc images. Relationships buit in 2019 were used to generate θ maps.

3. Results

3.1. Establishment of non-water stressed baseline and non-transpiring baseline

Diurnal patterns for OP and RD treatments for the two representative stressed days (24th July 2018 and 29th June 2019) which were used to establish the lower, $(Tc - Ta)_{LL}$, and upper, $(Tc - Ta)_{UL}$, baselines for the empirical single-day method, are presented in Fig. 3. 24th July 2018 was one day after RD irrigation (on 23 July) and five days after OP (on 19 July) events; hence RD was less stressed on this day, and thus was used to establish the $(Tc - Ta)_{LL}$. In 2019 on the other hand, OP with irrigations on 21 and 27 June and RD irrigation on 21 June representing stressed and unstressed conditions respectively on 29 June were used to establish appropriate $(Tc - Ta)_{LL}$ and $(Tc - Ta)_{UL}$. Linear regression models were fitted for the negative Tc -Ta / VPD relationship for the unstressed crop between 9 and 17 h CEST for both years. Only slight differences exist for the slope and intercept in both years (Table 5) while

the R^2-values were significantly different from each other (2018: 0.83 and 2019: 0.98). The $(Tc - Ta)_{UL}$ were significantly different for each year but a suitable $(Tc - Ta)_{UL}$ could not be established in 2018 since the maximum Tc-Ta for OP which was stressed on this day was only 1.2 °C which is not a reasonable value for potatoes (Fig. 3).

The $(Tc - Ta)_{LL}$ equations fitted for the Tc -Ta / VPD relationships considering the multi-day method were significant for both years, with R^2 values 0.88 and 0.83 (p < 0.001; Fig. 4, Table 5) for 2018 and 2019 respectively. While the empirical $(Tc - Ta)_{LL}$ and $(Tc - Ta)_{UL}$ parameters derived from single-day and multi-day methods were significantly different from each other, they were relatively invariant between years when each method is considered individually. The $(Tc - Ta)_{UL}$ and R^2 from the multi-day method were very similar to each other (Table 5) and could be more useful in establishing suitable baselines for application across multiple years. Given this advantage and the higher stability that is provided by multi-day methods (Gardner et al., 1992), the final CWSIe was estimated from limits derived from the multi - day method. Additionally, the mean value of $(Tc - Ta)_{UL}$ from 2018 and 2019 multi-day method, 5.7 °C, was used to calculate CWSIh, which is close to the value (5 °C) used by Gerhards et al. (2016) for potato crops in Germany.

Derived $(Tc - Ta)_{UL}$ and $(Tc - Ta)_{LL}$ from the three CWSI models (CWSIe, CWSIt and CWSIh) are presented in Fig. 5. As previously mentioned, $(Tc - Ta)_{UL}$ used for the hybrid method was the mean $(Tc - Ta)_{UL}$ from the multi - day empirical method for 2018 and 2019 hence they are only slightly different from the empirical upper limits in both years. For the theoretical method, only the mean $(Tc - Ta)_{UL}$ is shown as it has a different value for each data point. The $(Tc - Ta)_{LL}$ values from the theoretical and hybrid models have similar curved patterns with higher scatter and lower values than those of the empirical method. The effect of the different limits affects the final CWSI models values. Since the lower baseline $(Tc - Ta)_{LL}$ for CWSIe was derived as the average of real Tc - Ta values on 17 days (2018) resp. 11 days (2019) with well-watered condition for the reason of numerical stability, its values are higher than the virtual Tc – Ta of an ideal optimally watered crop.
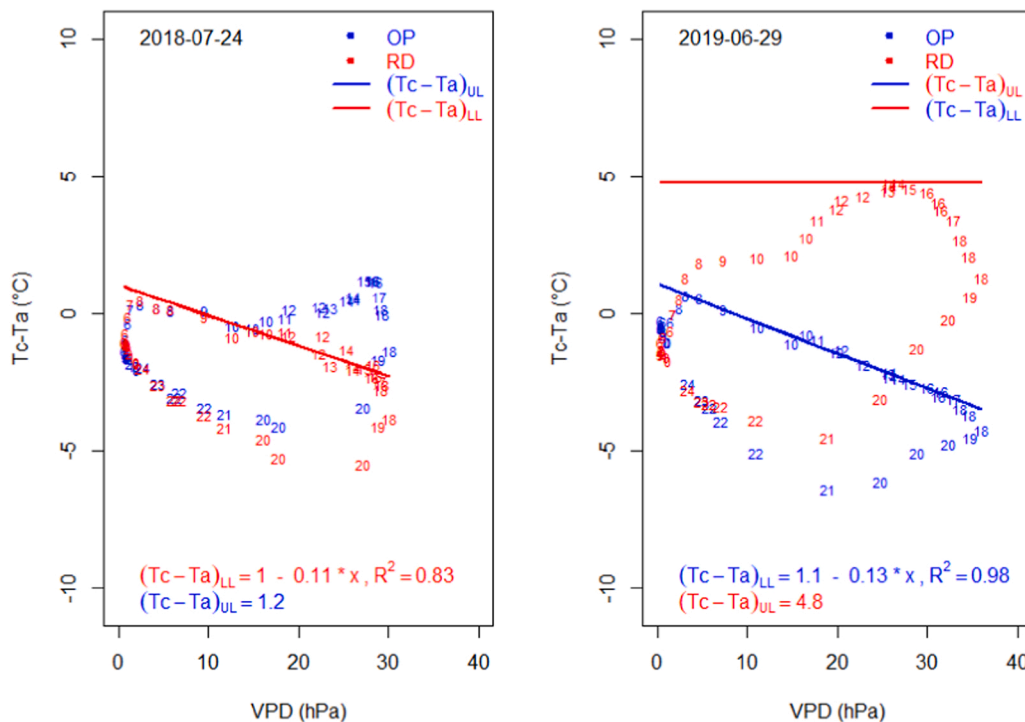

Fig. 3. Linear relation between Tc-Ta and VPD to determine non-water-stressed baseline for single -day method, numbers denote the hour of day. In 2019 (right), conditions to determine LL and UL were ideal. In 2018 (left), RD was irrigated one day before the measurements, so it can be considered as fully irrigated (and thus, was used to determine the LL) whereas the OP was irrigated five days before and only exhibited light drought stress (thus, no UL is plotted). The NWSB (Tc-Ta)LL in both years show similar equations.

Table 5

Derived upper and lower baseline equations for the estimation of empirical CWSI. All relationships were significant with p values < 0.001.

Method	Year	Day (DOY)	Number of Days	$(Tc\text{-}Ta)_{LL}$	$(Tc\text{-}Ta)_{UL}$	R^2
Single - Day	2018	24 July (205)	–	1.0-0.11 *VPD	1.2	0.83
	2019	29 June (180)	–	1.1-0.13 *VPD	4.8	0.98
Multi - day	2018	–	17	3.6–0.22 *VPD	5.67	0.88
	2019	–	11	3.3–0.26 *VPD	5.35	0.83
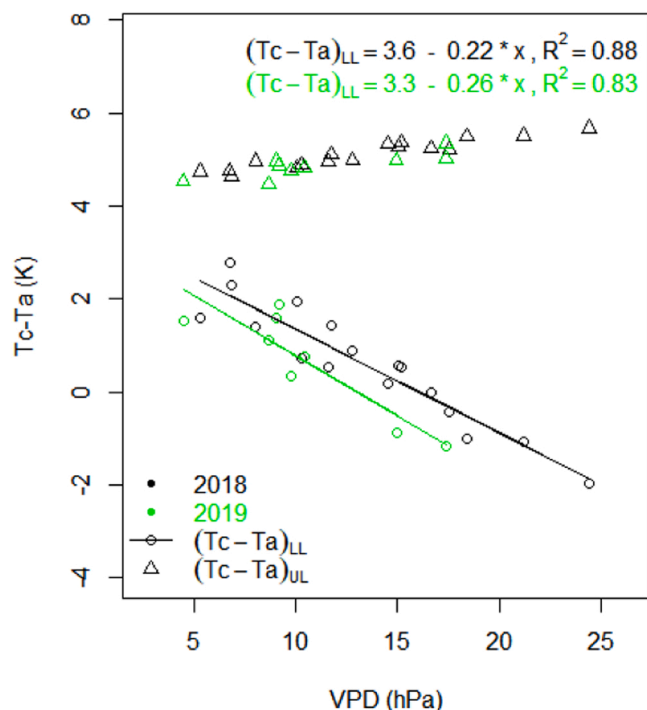
Fig. 4. Estimated lower and upper limits for calculating empirical CWSI (11–15 h CEST) according to the multi-day method. The equations for LL and UL show similar equations in both years.

3.2. Relationships between soil water content and CWSI

Volumetric soil water content (θ) measurements were used as the basis to assess the suitability of the different CWSI models to represent stress conditions. The temporal dynamics of θ at 10 cm and 20 cm depth showed good correspondence with both rain and irrigation events (Fig. 6), with θ values increasing sharply after each irrigation or rain event and slowly decreasing with soil drying until the next event. In 2018, θ at 10 and 20 cm depth showed similar variability while in 2019, θ at 10 cm depth was more variable than θ at 20 cm depth. This is likely due to the measurement position of the sensors. Previous unpublished research work of LWK revealed that only little irrigation water percolates under the top of the ridge. In 2018, maximum and minimum θ values for OP and RD mostly had the same magnitude throughout the season. In 2019 however, absolute θ values of the OP treatment remained above the θ values of the RD treatment.

The seasonal course of daily midday (from 11h to 15h CEST) values of the three CWSI models together with θ, irrigation and significant rain (> 5 mm) events in 2018 are examined (Fig. 7). All CWSI models showed expected variations with respect to soil water content, irrigation and rain. However, the pattern is not observable throughout the season but can be seen only at certain periods. Only periods with relatively high Rg and VPD (Rg > 600 Wm^{-2} and VPD > 20hPa; grey background Fig. 7) have this response implying that the crop must experience high radiative heating and atmospheric demand for the expected CWSI responses to occur. Considering only these periods, mean CWSI values for RD were marginally higher than for OP irrigation with values for CWSIe, CWSIt and CWSIh being 0.18, 0.34 and 0.49 and 0.15, 0.32 and 0.47 respectively (Table 6). The effect of higher (Tc - Ta)$_{LL}$ for CWSIe method (Section 3.1; Fig. 5) can be seen in its significantly smaller mean values compared to CWSIt and CWSIh. Most Tc-Ta values fall below the (Tc - Ta)$_{LL}$ causing most of CWSIe values to be negative and lowering the mean values.

In Fig. 7 upper plot (RD), in the dry period between DOY 190 and DOY 204 an inverse relationship between soil moisture (SM) and CWSI can be observed: At DOY 190, SM is high (25%, blue circle) and corresponding CWSI values are low at values close to or below 0 (red triangle, black dot, green dot). Then during this dry period, SM declines from 25% to 7% (at DOY 204), while CWSI increase to values around 0.4–0.7 (depending on CWSI type). Similar behaviour is present in the same plot for period DOY 170–182 or in the Fig. 7 lower plot (OP) during period DOY 190–204.

Similar seasonal dynamics in θ and daily midday CWSI models are
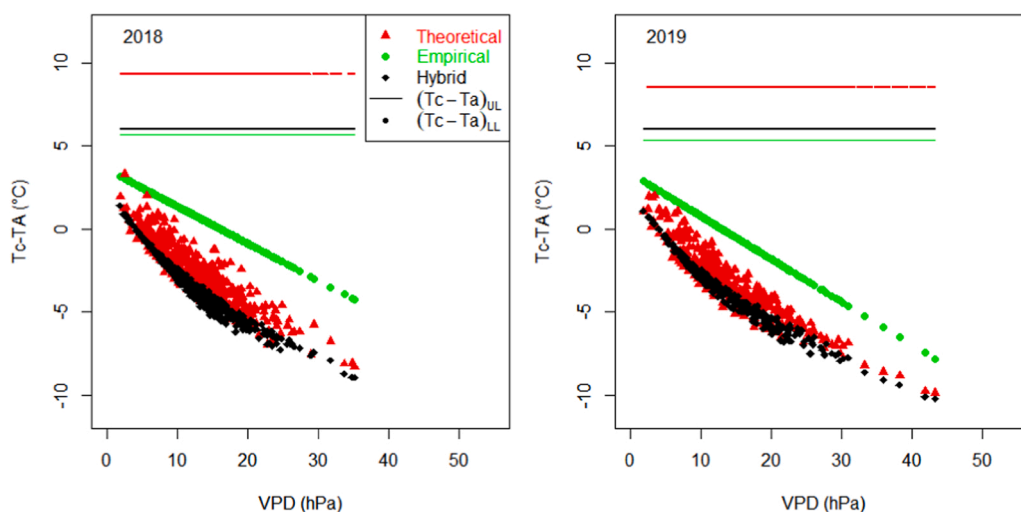

Fig. 5. Comparison of upper - (Tc - Ta)$_{UL}$ and lower - (Tc - Ta)$_{LL}$ limits from the empirical, theoretical hybrid models.
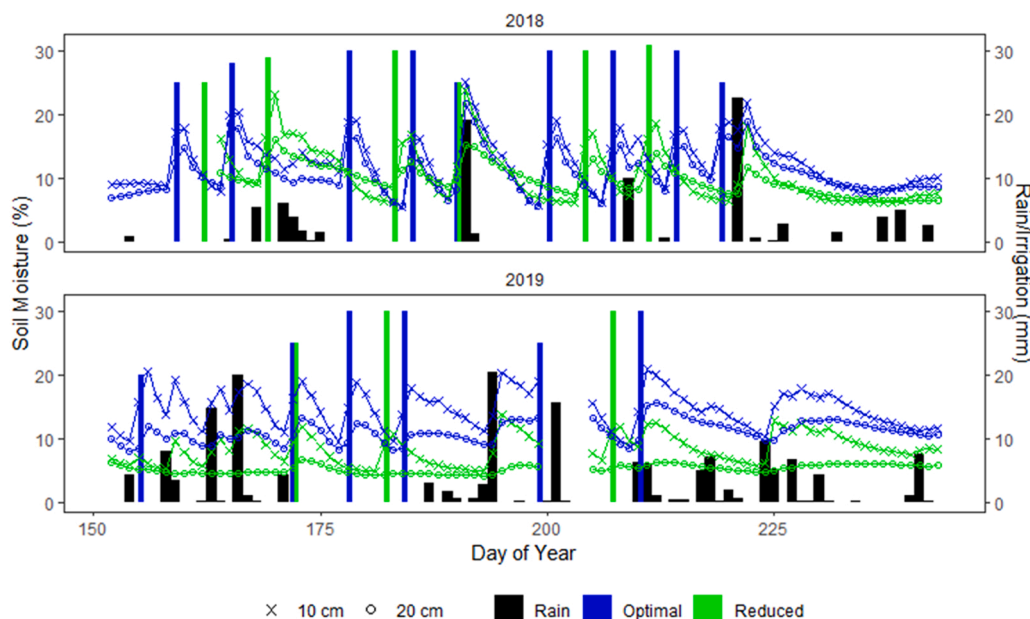
Fig. 6. Temporal evolution of the midday soil water content in 10 cm and 20 cm depth together with rain and irrigation events in 2018 (top) and 2019 (bottom).
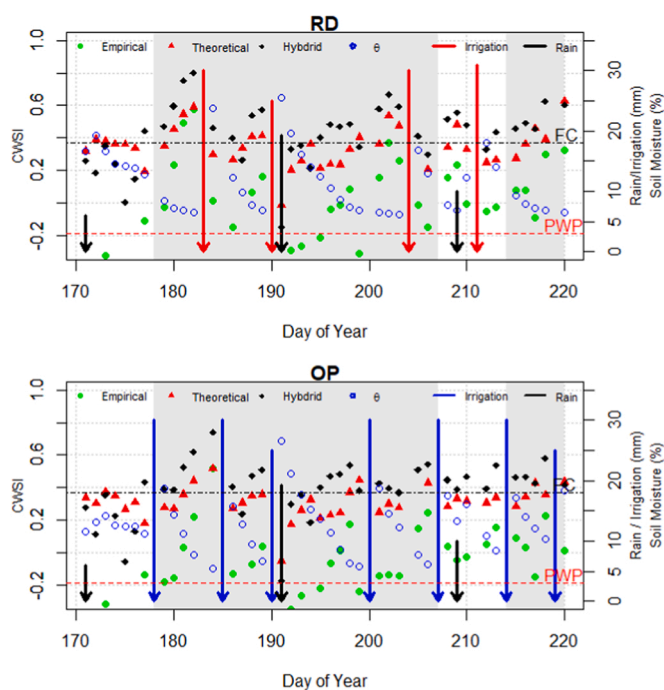

Fig. 7. Seasonal evolution daily midday (11–15 h CEST) soil water content at 10 cm depth (θ), empirical CWSI (CWSIe), theoretical CWSI (CWSIt), hybrid CWSI (CWSIh) for the reduced (RD, above) and optimal (OP, below) irrigation plots, together with corresponding soil water content (θ), irrigation events, and significant rain (> 5 mm) for 2018. Grey background indicates periods of high incoming solar radiation where inverse relations between CWSI and θ can be observed during absence of rain or irrigation (e.g. period DOY 190–204). FC and PWP lines only apply to the right-hand axis.

also observed in 2019 (Fig. 8), with higher CWSI values (Table 6) for RD (CWSIe = 0.5, CWSIt = 0.46, CWSIh = 0.61) than OP (CWSIe = 0.26, CWSIt = 0.32, CWSIh = 0.45). Like in 2018, only periods with relatively high Rg and VPD show good response, however the length of these

Table 6
Mean and standard deviations (in brackets) for midday (11–15 h) Tc, CWSIe, CWSIt and CWSIh for days with mean Rg > 600 Wm^{-2} and VPD > 20hPa.

2018			2019		
Index	RD	OP	Index	RD	OP
Tc	29.19 (2.04)	28.98 (2.03)	Tc	31.92 (2.63)	29.46 (2.32)
CWSIe	0.18 (0.19)	0.15 (0.17)	CWSIe	0.50 (0.20)	0.26 (0.14)
CWSIt	0.34 (0.14)	0.32 (0.08)	CWSIt	0.46 (0.12)	0.32 (0.10)
CWSIh	0.49 (0.11)	0.47 (0.09)	CWSIh	0.61 (0.13)	0.45 (0.08)
θ	10.55 (4.20)	14.88 (7.76)	θ	6.53 (2.10)	13.09 (2.35)

periods were shorter and limited in 2019. Two periods where such patterns are clearly visible are the periods from 20 June - 3rd July (DOY 171–184; grey background in Fig. 8) and 23–28 th July 2019 (DOY 204–209; grey background in Fig. 8).

Pearson correlation coefficients (r) between Tc and the three different CWSI models at midday (11:00 – 15:00 h CEST) and θ at 10 cm depth are shown in Table 7. To show the effects of the meteorological conditions on thermal measurements, correlations are shown for all the observations and periods when Rg > 600 Wm^{-2} and VPD > 20hPa (grey background Fig. 7 & 8). Correlation coefficients are also shown for all irrigation treatments (RD & OP) combined and when they are considered separately. For all considerations, r was higher for periods with Rg > 600 Wm^{-2} and VPD > 20hPa than when all observations are considered. Also, r was higher for RD than OP treatments for both years, although better correlations exist for RD & OP and RD in 2019 than 2018.

3.3. Estimating of θ from CWSI

Scatter plots of mean daily midday Tc and CWSI vs 10 cm θ are presented in Fig. 9. From the scatter plots and summary statistics (Table 6), it can be observed that θ and index values for OP and RD treatments were not significantly different from each other in 2018, while clear distinctions exist between RD and OP θ in 2019 hence Tc and all CWSI models were different from each other. R^2 values were poor in 2018 ($R^2 < 0.4$) and good in 2019 ($R^2 \approx 0.6$) even for Tc. A comparison
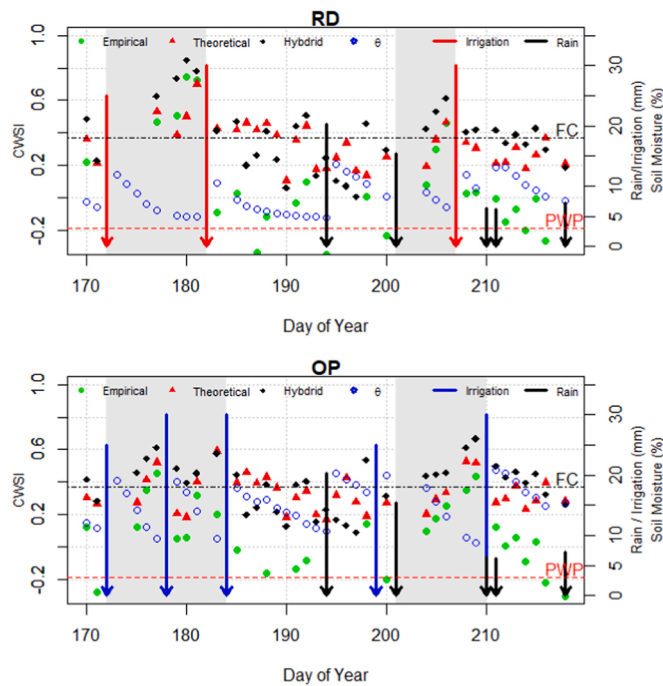
Fig. 8. Seasonal evolution daily midday (11–15 h CEST) soil water content at 10 cm depth (θ), empirical CWSI (CWSIe), theoretical CWSI (CWSIt), hybrid CWSI (CWSIh) for the reduced (RD, above) and optimal (OP, below) irrigation plots, together with corresponding soil water content (θ), irrigation events, and significant rain (> 5 mm) for 2019. Grey background indicates periods of high incoming solar radiation where good patterns of CWSI and θ can be observed.

Table 7
Correlation coefficients (r) between midday (11–15 h) 10 cm θ and Tc, CWSIe, CWSIt and CWSIh.

2018							
	All Days			**Rg > 600 Wm-2 and VPD > 20hPa**			
Index	**RD & OP**	**RD**	**OP**	**Index**	**RD & OP**	**RD**	**OP**
Tc	-0.21	-0.29	-0.10	Tc	-0.37	-0.44	-0.31
CWSIe	-0.39	-0.44	-0.29	CWSIe	-0.60	-0.73	-0.50
CWSIt	-0.40	-0.48	-0.23	CWSIt	-0.49	-0.71	-0.22
CWSIh	-0.41	-0.47	-0.31	CWSIh	-0.61	-0.76	-0.50
2019							
Tc	-0.11	-0.32	-0.10	Tc	-0.68	-0.70	-0.55
CWSIe	-0.13	-0.35	-0.21	CWSIe	-0.76	-0.67	-0.60
CWSIt	-0.23	-0.51	-0.32	CWSIt	-0.77	-0.81	-0.57
CWSIh	-0.16	-0.36	-0.23	CWSIh	-0.77	-0.65	-0.57

between the predicted θ and measured θ is presented in Fig. 10. Predicted θ for 2018 from relationships in 2019 were generally better (R^2 > 0.5; RMSE < 2%) for all CWSI models while predictions of 2019 from 2018 were poor (R^2 < 0.4; RMSE > 2%). For both cases considered in Figs. 9 and 10 CWSIe had the best performance for both models.

3.4. Application to thermal images

CWSIh was computed on the drone images replacing IRT-based Tc with drone-based Tc in Eq. 1. Environmental conditions during the drone flights are given in Table 8.

CWSIh maps for three experimental days, 19 June, 26 June and 24 July are shown in Fig. 11. Data collected on 24 August was not analysed further since most of the leaves were dried up by this date and images mostly captured soil temperature.

On the 19th of June, spatial variability of CWSI due to irrigation treatments is not reflected in the maps. However, on 26 June and 24 July, spatial patterns are clearly visible and reflect the corresponding irrigation. This confirms the previous results that spatial CWSI patterns can reflect the patterns of plant available soil water. The visibility of spatial patterns on 26 June and 24 July (but not on 19 June) is due to absence of rain in the period before image acquisition and the high Rg and VPD (Table 8) on these days, which is necessary for stress detection with TIR. For accurate water stress detection, crops must heat up significantly (high Rg), and there must be high atmospheric demand (high VPD).

3.5. Potato yield results

Yield results are beyond the focus of this paper but are given in Table 9 for completeness of the presentation. Reduced irrigation resulted in a 15% yield reduction in 2018 and 10% yield reduction in 2019, compared to OP. Without any irrigation (control treatment), yield dropped to 40% of the OP treatment in the very dry year 2018, and to 57% in 2019.

4. Discussion

4.1. Non-water stressed baseline and non-transpiring baseline

The R^2 values from empirical equations to derive the NWSB ((Tc - Ta)$_{LL}$) and NTB ((Tc - Ta)$_{UL}$) from the single-day and multi-day methods are within acceptable limits for both methods. Gardner (1992b) reported that for single-day methods, R^2 values should typically be greater than 0.95 while for multi-day methods R^2 values around 0.6 and 0.7 are acceptable. Recent studies such as Taghvaeian et al. (2012) and Berni et al. (2009) had R^2 values of 0.98 and 0.67 for single and multi-day methods respectively. Nevertheless, R^2 value for the (Tc - Ta)$_{LL}$ in 2018 was 0.83, less than 0.98 obtained in 2019. Differences in slope and intercept were also recorded between both years (2018 & 2019). Differences between consecutive years for the same crop in the same place have also been reported in other studies; Gonzalez-Dugo et al. (2014) reported different values for intercept, slope and R^2 for their three-year experiment, 2009, 2010, 2011 for mandarin and orange trees, DeJonge et al. (2015) and Taghvaeian et al. (2012) made similar observations for maize. Such differences have been attributed to climatic conditions between different years, crop growth stages, differences in transpiration rate and water uptake potential between years and instrument parameters such as IRT view angles (Gonzalez-Dugo et al., 2014; Han et al., 2018). In this study the differences in climatic conditions (2018 was drier than 2019) and crop growth stage (suitable day for single-day empirical method in 2018 was 24 July which was at late stages of tuber development while 2019 was 29 June which was in the flowering stage; Table 2) likely caused the differences in slope and intercept.

The (Tc - Ta)$_{UL}$ were significantly different for each year which could be attributed to the level of stress and the amount of radiation available on the selected days. The stressed crop in 2019 had three additional days of stress compared to 2018. The low (Tc - Ta)$_{UL}$ of 2018 (1.2 °C) from the single - day method does not represent the maximum stress conditions for potatoes because the OP irrigation was not under severe stress, hence cannot be used as a reliable (Tc - Ta)$_{UL}$. In such cases where a reliable upper limit cannot be derived from irrigation treatments and no other data is available a constant (Tc - Ta)$_{UL}$ value of 5.0 °C is recommended
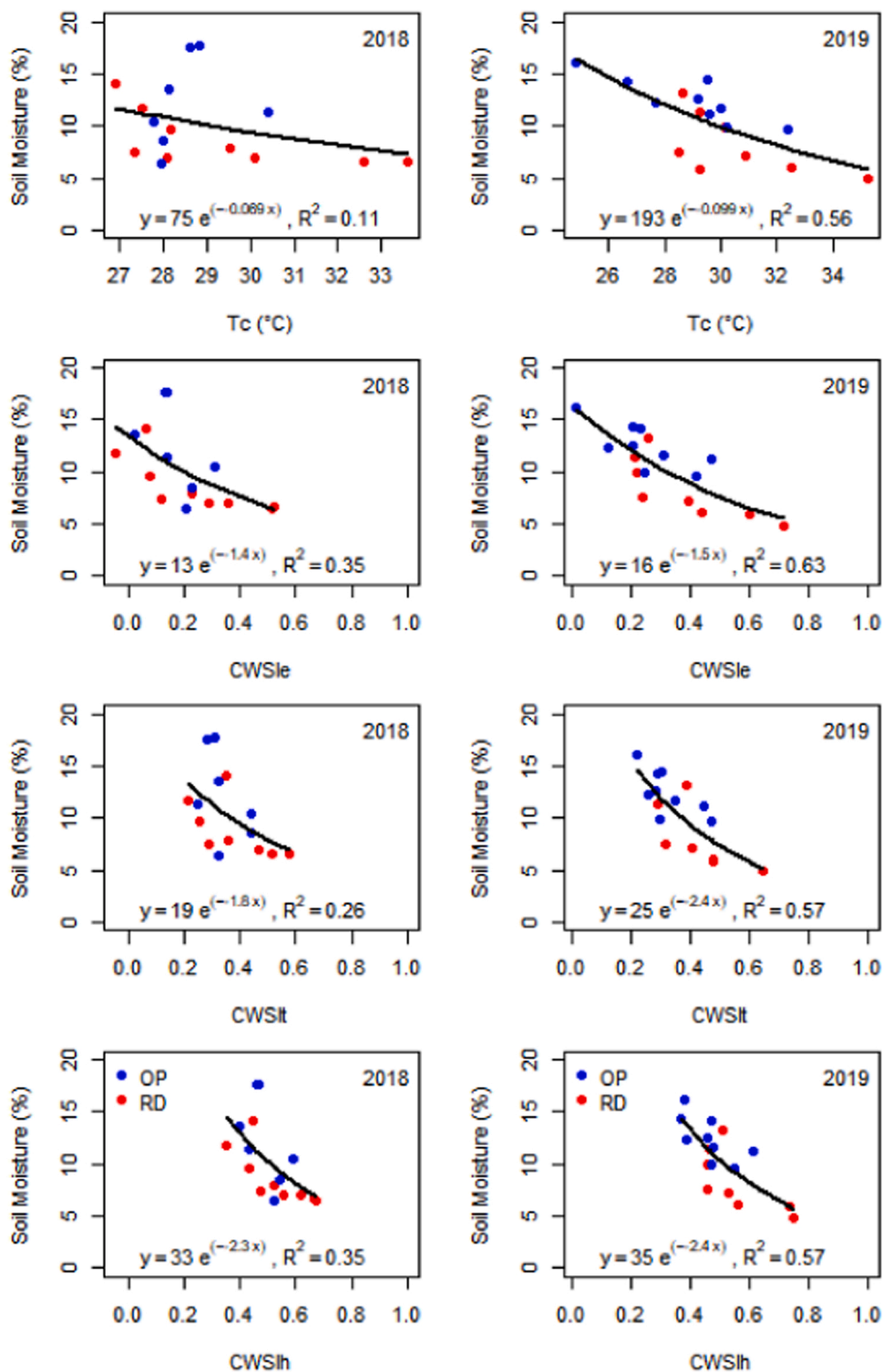
Fig. 9. Relationship between mid- day index vs soil water content at 10 cm (%) when Rg > = 600 W/m^2 and VPD > = 20 hPa for 2018 (left column) and 2019 (right column).

for use (Taghvaeian et al., 2014). Typically, (Tc - Ta)$_{UL}$ is derived from severely stressed crops under ideal conditions (Idso et al., 1981; Irmak et al., 2000; DeJonge et al., 2015), however Al-Faraj et al. (2001) observed that this may not be suitable for all cases even under controlled experiments, hence the application of the baseline equation (Eq. 3)

comes in handy in such cases. Also, the use of mean and maximum upper limit values for CWSIt and CWSIe as indicated in Fig. 5 has been widely applied.

The higher (Tc - Ta)$_{LL}$ values from the empirical method presented in Fig. 5 can be attributed to the experimental setup where OP and RD
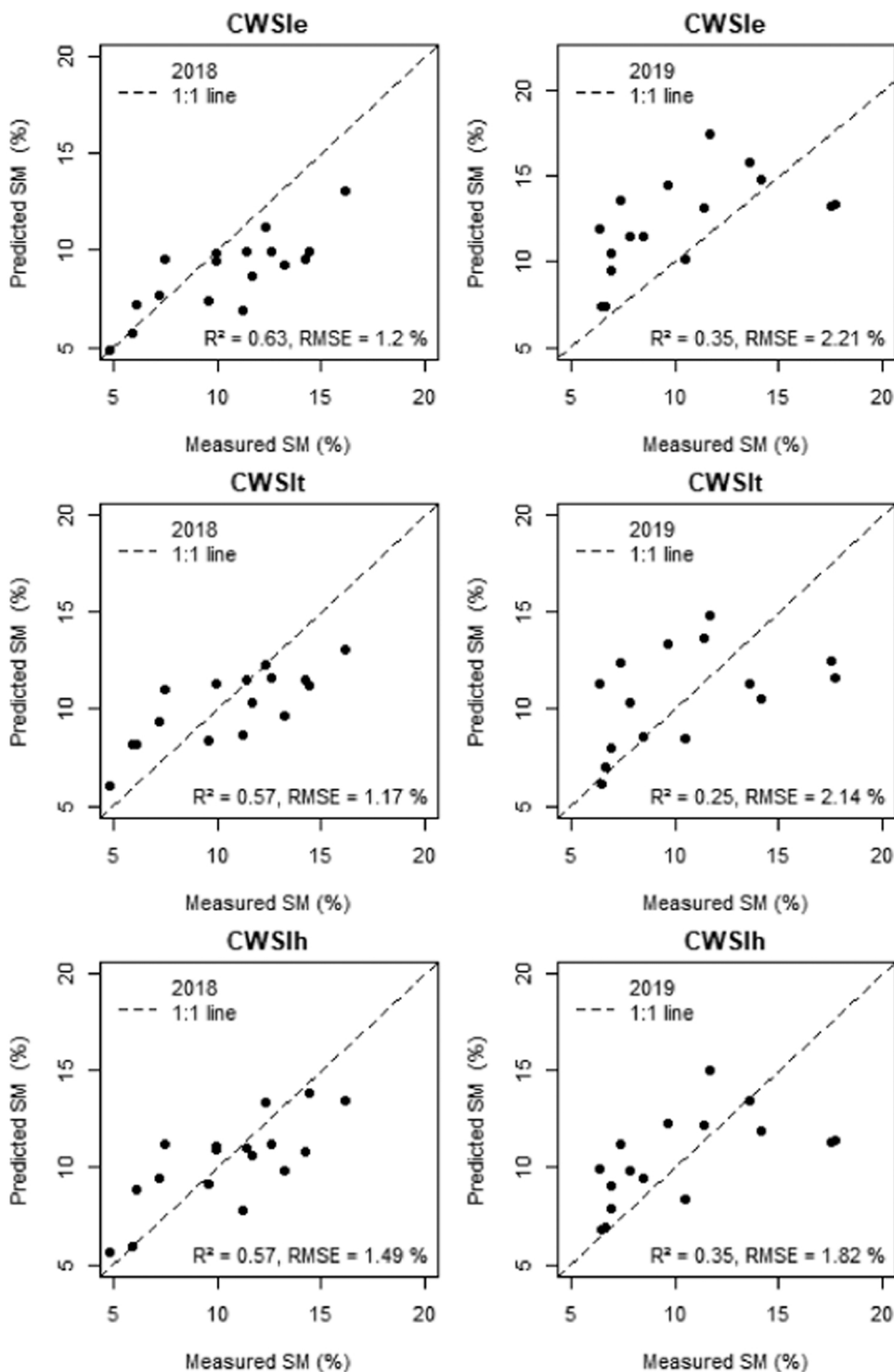
Fig. 10. Performance of predicted soil water content at 10 cm (%) for 2019 from relationships derived in 2018 (left column), and for 2018 from relationships derived in 2019 (right column). Dashed lines represent 1 on 1 line.

Table 8
Acquisition dates and time of thermal imagery and atmospheric conditions at time of UAV flight.

TIME	Rg (Wm^{-2})	Ta (°C)	VPD (hPa)
19/06/2019 13:45	531.38	29.44	22.40
26/06/2019 15:15	701.67	31.71	26.24
24/07/2019 14:10	741.72	31.38	26.70

irrigation amounts are set at 50% and 35% field capacity respectively. Typically, the (Tc - Ta)$_{LL}$ is derived from irrigation treatments with 100% plant available water or field capacity resulting in much lower (Tc - Ta)$_{LL}$ values. The irrigation treatments in this experiment therefore cannot represent conditions for well-watered crops and the derived parameters may be suboptimal as reported by Al-Faraj et al. (2001) in *tall fescue,* although Irmak et al. (2000) had obtained suitable lower baselines for corn even at 50% available water holding capacity, which
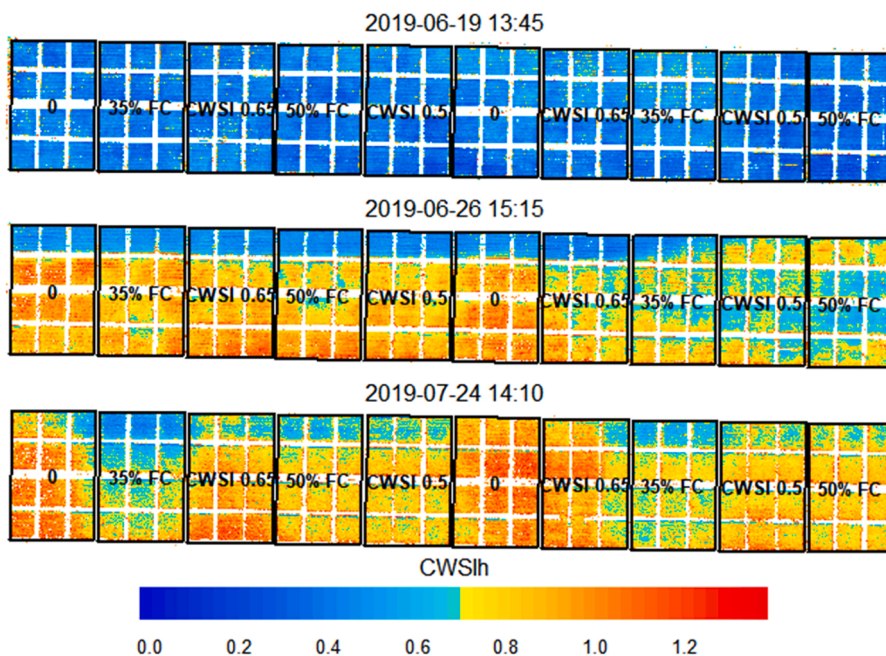
Fig. 11. CWSIh for potato field. Labels are irrigation treatments applied to the plots, i.e., Reduced (CWSI 0.65, 35% FC), Optimal (CWSI 0.5, 50% FC), and No Irrigation (0).

Table 9
Potato tuber yield results.

	OP	RD	Control
2018	66.1 t/ha	56.2 t/ha	26.4 t/ha
2019	64.0 t/ha	57.6 t/ha	36.5 t/ha

was expected to be the case in this study since within the first two days after 20–30 mm irrigation (Table 2), the water availability was unrestricted for both of the treatments.

4.2. Soil water content - CWSI relations

The results from the conducted analysis demonstrate that CWSI models can be used to monitor crop and soil water status and dynamics. CWSI was expected to be high during water stress (low θ) and decrease during recovery (after rain/irrigation), additionally OP treatments were also expected to be less stressed than RD irrigation treatments. Both expectations are generally met in this study for all three models. However, good CWSI dynamics and correlations are only observable/obtained under certain meteorological conditions with high Rg and VPD during high radiative heating and high atmospheric demand (Table 7).
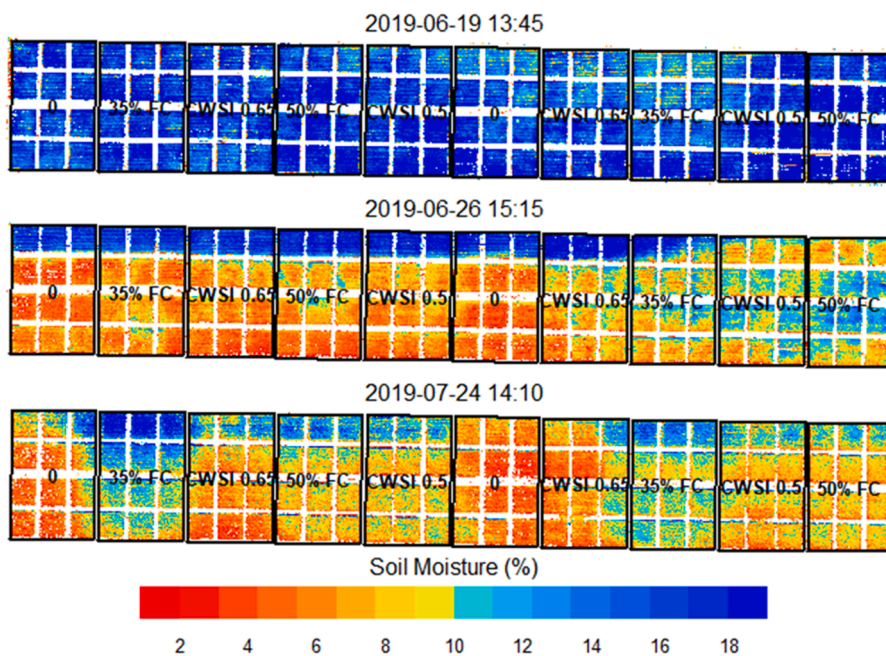

Fig. 12. Estimated soil water content (%) for potato field based on the calibration between CWSIt and soil water content at 10 cm (Fig. 9). Labels are irrigation treatments applied to the plots, i.e., Reduced (CWSI 0.65, 35% FC), Optimal (CWSI 0.5, 50% FC), and No Irrigation (0). Approx. 3–4 Vol% corresponds to PWP, 15–18 Vol% to FC.

Poor dynamics and correlations for the whole study period is due to the presence of cloudy conditions with low Rg and VPD on certain days and the relationships greatly improve under "dry" conditions only (high Rg and VPD). Similar results have also been documented by Agam et al. (2013a).

Important requirements in obtaining strong CWSI-θ relationships are the accurate measurement of soil water content and variation from dry to wet conditions. In this experiment, soil water content measurements for 2018 and 2019 were carried out at two different locations. In 2018 the soil moisture sensors were placed in the valley between two ridges and in 2019, soil moisture measurements were done at the top of the ridge where the potato plant grows. The effect of this disparity can be seen in Fig. 6 where the difference in 10 and 20 cm soil water content for 2018 were mostly the same while for 2019 there is a huge difference in soil water content between both depths. Irrigation water (and rain) applied at the top of the ridge tends to infiltrate mainly into the valley. The infiltration on the top of the ridge is much less and mostly restricted to the top centimetres of the ridge hence high variability of soil at the 10 cm depth while the 20 cm is more stable.

It would be desirable to provide a soil water content threshold for beginning water stress. This is however difficult to estimate as the choice of CWSI model affects the results, and due to limits in measurement accuracy, CWSI is rarely exactly 0 even for unstressed vegetation. The most reliable method in this case would be to treat a certain percentile of the lowest CWSI values observed in a season as "unstressed". From the data shown in Fig. 9, this seems to be around 12–15% volumetric soil water content, which corresponds to a depletion fraction for no stress similar to FAO56 of $0.2 - 0.4$ (assuming PWP=3% and FC=18%), which is somewhat lower than the FAO56-recommended value of 0.35 for potatoes (Allen et al., 1998).

4.3. Comparison of CWSI models

Several studies have shown that CWSI is a better indicator of water stress than Tc (Berni et al., 2009; Gerhards et al., 2019). However, while this was the case in 2018, the CWSI models did not provide significant improvement for 2019, an observation which was also made by DeJonge et al. (2015). With respect to the different CWSI models, some studies comparing the different models have shown CWSIe to perform better than CWSIt (Agam et al., 2013b; Liu et al., 2020) and others have shown similar performance for CWSIe and CWSIt for olives (Ben-Gal et al., 2009) and for potato in particular (Rud et al., 2014). In this study, CWSIe performed slightly better than CWSIt and CWSIh in representing and predicting soil water content. Improvements in CWSIt can be made by using a seasonal average r_A, which can reduce uncertainty for the different growth stages and instantaneous atmospheric effects (Jackson et al., 1988; Han et al., 2018).

Although it is expected that CWSI should be a better indicator than direct Tc, DeJonge et al. (2015) found out that Tc measurements alone without meteorological parameterization, were equally capable as CWSI in representing soil moisture deficit under certain conditions and can be used for such instances. However, CWSI models are still advantageous as they consider meteorological variables and scale the value of stress to quantifiable limits of stress $(0-1)$ unlike simple Tc measurements where no absolute limits of stress can be established which is important in practical irrigation scheduling and water stress monitoring situations. All meteorological measurements required for estimating CWSI might not be readily available (Berni et al., 2009) and in addition to the limitations of both CWSIe and CWSIt outlined in Section 1, the use of CWSIh could be a suitable alternative given that it could easily be applied without further calculations of aerodynamic resistance r_A and net radiation. Additionally, CWSIh combines the best aspects of CWSIe and CWSIt and has been recommended by Agam et al. (2013b) as a more practical method for daily monitoring of stress and shown to work well for stress monitoring in potatoes (Rud et al., 2014;). Nevertheless, some level of caution should be observed when assigning fixed upper limit

values as index values are sensitive to such values (Agam et al., 2013b).

The good level of θ predictions from the CWSIe and CWSIh models (mainly in 2019) demonstrate that these indices can be used to simulate and predict irrigation amounts from one year to another, when similar meteorological and soil moisture conditions prevail. Also in other research the use of CWSI-θ relations to simulate soil water content (θ) has been shown to provide reliable soil moisture estimates in the absence of in situ θ measurements (Taghvaeian et al., 2012; Liu et al., 2020).

4.4. Application to thermal images

In the present study, CWSI maps accurately captured the different levels of water stress which reflected the different irrigation treatments in the field although errors in derived Tc presumably led to errors in CWSI maps. CWSI values from images were generally larger than in situ CWSI values which eventually led to lower estimated soil water content. However, the accuracy of the final soil moisture maps could not be ultimately verified due to lack of sufficient spatially distributed in situ field measurements.

Tc values were generally higher in the images than in situ Tc (by about 2.1 °C). Errors in Tc from remote sensing images have been attributed to atmospheric effects, differences in view angles and accuracy of drone TIR sensors and field thermometers (Song and Park, 2020). Heinemann et al. (2020) stressed the importance of accurate estimation of specific emissivity, consideration of environmental background temperature and atmospheric transmittance to obtain Tc with errors less than 0.05 K. Additionally, co-registration inaccuracies between TIR and VNIR images used for extraction of pure Tc may lead to pollution by background signals in the final Tc image. Although various methods of separation of pure Tc from background signals of soil and plant shadow exist (Wang et al., 2010; Meron et al., 2013) and were applied to the images, no method has been shown to be completely perfect for pure Tc extraction (Zhang et al., 2019). Zhang et al. (2019) also suggested that TIR images could be recalibrated using coefficients derived from linear relationships within situ Tc measurements, however this method has not been widely applied yet and was not used in the current study.

Relationships derived from in situ measurements and applied to CWSI maps for spatial monitoring have been shown to work well in predicting spatial variations of stress. For instance, Berni et al. (2009) produced accurate CWSI maps from canopy conductance derived from high spatial resolution UAV thermal imagery and relationships with CWSI have been used to map leaf water potential (Cohen et al., 2005, 2017). Such maps may be used to estimate available soil water within the crop's root zone so that soil water deficit can be quantified within the field for irrigation scheduling (Padhi et al., 2012).

4.5. Spatial variations within CWSI and SM (soil moisture) images

On June 19 (Fig. 11, top map), there was no water stress despite hot midday temperatures due to 20 mm of rain four days before. Soil water content was about 50–70% field capacity (FC) equivalent to 10.5–13.5 volume % (Fig. 12, top map). June 26 was five days after the last irrigation for both OP and RD plots and the previous days were hot and dry with presumably high transpiration rates. On the left (Western) side of the field, intensive drought stress (Fig. 11, centre map) and low soil water content (Fig. 12, bottom map) can be observed even in the 50% FC plots. In contrast on the right (Eastern) side of the field, in the same treatment class (50% FC) only mild drought stress and intermediate soil water content values can be observed. A possible explanation are differences in soil properties, for instance loamy lower soil layers with larger water holding capacity than the otherwise prevalent sandy layers. From the loamy soil horizon plants can be supplied with water and show less drought stress, despite the topsoil layer being very dry. These soil properties tend to increase towards the Eastern part (right side in Figs. 11 and 12) of the field. Smaller areas of mild drought stress can also

be seen in the Western part of the field. These interpretations are supported by analysing the yield of the individual parcels (not shown), where the yield for the assumed better soil (with larger soil water holding capacity) in the East end was larger by 10–20% compared with the West end in both treatment variants CWSI 0.5 and FC 50%. Similar differences in soil properties in the same agricultural field have also been observed by Padhi et al. (2012) and Han et al. (2018) which also accounted for the differences in soil water distribution, crop growth and crop response to drought stress. An alternative explanation could be that in the stressed (red coloured) areas unfavourable soil properties or poorly developed plants have decreased the rooting depth such that less water can be absorbed by the soil. However, those areas seem too large to make this a likely cause.

The blue stripe at the top margin of the 26 June image indicates wind drift of water from the neighbouring field during irrigation. On 24 July (bottom maps in Figs. 11 and 12), we can see that the RD treatment (35% FC) plots have relatively low stress and large θ values. Indeed, those plots had been irrigated just two days before (Table 2) and were during the time of image capture at about 60–70% FC. One may notice a border effect from the neighbouring treatment caused by the used irrigation method (nozzle cart). The nozzles spray up to 9 m and can spray some of the water in the neighbouring parcel. For that reason, only the centre part of the parcel is harvested that receives the exact amount of irrigation water as planned. One can also notice an uneven water distribution within the parcels, likely due to wind drift by Southerly winds during the irrigation. On 24 July, the other RD treatment (CWSI 0.65) had not yet received irrigation and indicates severe drought stress and low soil water content (less than 30% FC). The OP treatments show intermediate drought stress at somewhat higher SM values compared to the CWSI 0.65 treatment. The 50% FC treatment was irrigated on the following day.

4.6. Suitability of thermal sensing in humid zones

The sensitivity of crop water stress index is affected by cloudy conditions hence the use of CWSI is valid only under clear sky conditions (Gardner et al., 1992a, 1992b; DeJonge et al., 2015). In humid regions however, the number of clear sky (high Rg) days are highly limited in wet years (2019; Fig. 8) compared to a dry year (2018; Fig. 7). This limits the use of CWSI in humid regions to periods with favourable atmospheric conditions. Even on days with high mean Rg, high hourly fluctuations in Rg due to clouds may lead to low CWSI values and an underestimation of stress (Agam et al., 2013a; Irmak et al., 2000).

Given these limitations, the use of an artificial wet (lower limit) and dry (upper limit) reference has been recommended by Jones (1999) in computing CWSI in humid regions. The approach is based on the concept that both reference surfaces change with corresponding change in canopy temperature under all atmospheric conditions. However, reference surfaces may not always be available and have been known to fail or disturbed by the meteorological factors (Jones, 1999; Gerhards et al., 2018; Bian et al., 2019). Alternatively, an adaptive CWSI algorithm has been developed by Osroosh et al. (2015) and has been shown to be effective in irrigation scheduling on cool and humid days. The algorithm estimates dynamic reference temperatures (upper and lower limits) which adjust for temporary weather conditions and avoid erroneous irrigation signals (Osroosh et al., 2015). Such a system can be tested and may prove useful in humid regions.

5. Conclusion

Irrigation experiments over two years were carried out to analyse the suitability of three crop water stress indices in monitoring water stress and assess their potential use in monitoring volumetric soil water content in humid/sub-humid environments. Results revealed that all CWSI models responded to variable irrigation treatments and showed good relationships with volumetric soil water content especially when irrigation experiments and measurements are properly done. In general, CWSIe models performed better than CWSIt and CWSIh. CWSI-θ relations calibrated in one year, could effectively predicted θ in another year with little errors of 1–2%. For practical purposes, CWSIh could be a promising alternative to the traditional CWSI (CWSIe and CWSIt) models since it requires the least amount of input variables.

The research demonstrates the propensity to accurately monitor field soil moisture conditions under "ideal" (i.e., high radiation, dry air) environmental conditions using TIR observations. The CWSI models could therefore be used for water stress monitoring and irrigation advice, thereby complementing or replacing traditional plant and soil water content measurements. In humid/sub-humid environments the possibility of application on a daily basis may however be limited by the limited number of cloud free days in a normal year. Although a few methods addressing this issue have been reported so far, more studies need to be carried out on their usefulness and new models need to be developed before CWSI can be widely used for stress monitoring and irrigation management in energy limited/humid zones.

With the future candidate TIR missions to space, the Copernicus LSTM (Land Surface Temperature Monitoring) and the NASA SBG (Surface Biology and Geology) missions, that will provide spatially continuous LST information at field scale, water stress indices are expected to face a wider application in agricultural water management applications.

CRediT authorship contribution statement

EK, MS, KM and FW conceived and designed the analysis; MK, AR and GR collected and pre-processed the data; EK, KM and MS contributed analysis tools; EK, MS, KM and FW performed the data analysis; EK and MS wrote the paper; MS, MK, AR and FW contributed to the revision of the manuscript.

Declaration of Competing Interest

The authors declare that they have no known competing financial interests or personal relationships that could have appeared to influence the work reported in this paper.

Acknowledgements

References

Agam, N., Cohen, Y., Alchanatis, V., Ben-Gal, A., 2013a. How sensitive is the CWSI to changes in solar radiation? Intern. J. Remote Sens. 34 (17), 6109–6120. https://doi.org/10.1080/01431161.2013.793873.

Agam, N., Cohen, Y., Berni, J.A.J., Alchanatis, V., Kool, D., Dag, A., Yermiyahu, U., Ben-Gal, A., 2013b. An insight to the performance of crop water stress index for olive trees. Water Manag. 118, 79–86. https://doi.org/10.1016/j.agwat.2012.12.004.

Al-Faraj, A., Meyer, G.E., Horst, G.L., 2001. A crop water stress index for tall fescue (Festuca arundinacea Schreb.) irrigation decision-making — a traditional method. Comput. Electron. Agric. 31, 107–124. https://doi.org/10.1016/S0168-1699(00)00182-4.

Allen, R., Pereira, L.S., Raes, D., Smith, M., 1998. Crop evapotranspiration-Guidelines for computing crop water requirements. FAO Irrigation and drainage paper 56.

Allen, R., Smith, M., Perrier, A., Pereira, L., 1994a. An update for the definition of reference evapotranspiration. ICID Bull. Int. Comm. Irrig. Drain. 43, 1–34.

Allen, R., Smith, M., Perrier, A., Pereira, L., 1994b. An update for the definition of reference evapotranspiration. ICID Bull. Int. Comm. Irrig. Drain. 43, 35–92.

Alvino, A., Marino, S., 2017. Remote sensing for irrigation of horticultural crops. Horticulturae 3, 40. https://doi.org/10.3390/horticulturae3020040.

Ben-Gal, A., Agam, N., Alchanatis, V., Cohen, Y., Yermiyahu, U., Zipori, I., Presnov, E., Sprintsin, M., Dag, A., 2009. Evaluating water stress in irrigated olives: correlation of soil water status, tree water status, and thermal imagery. Irrig. Sci. 27 (5), 367–376. https://doi.org/10.1007/S00271-009-0150-7.

Berni, J.A.J., Zarco-Tejada, P.J., Sepulcre-Cantó, G., Fereres, E., Villalobos, F., 2009. Mapping canopy conductance and CWSI in olive orchards using high resolution thermal remote sensing imagery. Remote Sens. Environ. 113, 2380–2388. https://doi.org/10.1016/j.rse.2009.06.018.

Bian, J., Zhang, Z., Chen, J., Chen, H., Cui, C., Li, X., Chen, S., Fu, Q., 2019. Simplified evaluation of cotton water stress using high resolution unmanned aerial vehicle thermal imagery. Remote Sens. 11, 267. https://doi.org/10.3390/rs11030267.

Cohen, Y., Alchanatis, V., Meron, M., Saranga, Y., Tsipris, J., 2005. Estimation of leaf water potential by thermal imagery and spatial analysis. J. Exp. Bot. 56, 1843–1852. https://doi.org/10.1093/jxb/eri174.

Cohen, Y., Alchanatis, V., Saranga, Y., Rosenberg, O., Sela, E., Bosak, A., 2017. Mapping water status based on aerial thermal imagery: comparison of methodologies for upscaling from a single leaf to commercial fields. Precis. Agric. 18, 801–822. https://doi.org/10.1007/s11119-016-9484-3.

Dalla Costa, L., Delle Vedove, G., Gianquinto, G., Giovanardi, R., Peressotti, A., 1997. Yield, water use efficiency and nitrogen uptake in potato: the influence of drought stress. Potato Res. 401 (40), 19–34. https://doi.org/10.1007/BF02407559.

DeJonge, K.C., Taghvaeian, S., Trout, T.J., Comas, L.H., 2015. Comparison of canopy temperature-based water stress indices for maize. Agric. Water Manag. 156, 51–62. https://doi.org/10.1016/j.agwat.2015.03.023.

Deng, Z., 2015. Examination of hydrodynamic soil-plant water relations with a new SPAC model and remote sensing experiments. Flinders University, Australia.

Fuentes, S., De Bei, R., Pech, J., Tyerman, S., 2012. Computational water stress indices obtained from thermal image analysis of grapevine canopies. Irrig. Sci. 306 (30), 523–536. https://doi.org/10.1007/S00271-012-0375-8.

Gardner, B.R., Nielsen, D.C., Shock, C.C., 1992a. Infrared thermometry and the crop water stress index. I. History, theory, and baselines. J. Prod. Agric. 5, 462–466. https://doi.org/10.2134/jpa1992.0462.

Gardner, B.R., Nielsen, D.C., Shock, C.C., 1992b. Infrared thermometry and the crop water stress index. II. Sampling procedures and interpretation. J. Prod. Agric. 5, 466–475.

Gerhards, M., Rock, G., Schlerf, M., Udelhoven, T., 2016. Water stress detection in potato plants using leaf temperature, emissivity, and reflectance. Int. J. Appl. Earth Obs. Geoinf. 53, 27–39. https://doi.org/10.1016/j.jag.2016.08.004.

Gerhards, M., Schlerf, M., Mallick, K., Udelhoven, T., 2019. Challenges and future perspectives of multi-/hyperspectral thermal infrared remote sensing for crop water-stress detection: a review. Remote Sens. 11, 1240. https://doi.org/10.3390/RS11101240.

Gerhards, M., Schlerf, M., Rascher, U., Udelhoven, T., Juszczak, R., Alberti, G., Miglietta, F., Inoue, Y., 2018. Analysis of airborne optical and thermal imagery for detection of water stress symptoms. Remote Sens. 10, 1139. https://doi.org/10.3390/rs10071139.

Gonzalez-Dugo, V., Zarco-Tejada, P., Nicolás, E., Nortes, P.A., Alarcón, J.J., Intrigliolo, D.S., Fereres, E., 2013. Using high resolution UAV thermal imagery to assess the variability in the water status of five fruit tree species within a commercial orchard. Precis. Agric. 14, 660–678. https://doi.org/10.1007/s11119-013-9322-9.

Gonzalez-Dugo, V., Zarco-Tejada, P.J., Fereres, E., 2014. Applicability and limitations of using the crop water stress index as an indicator of water deficits in citrus orchards. Agric. . Meteorol. 198–199, 94–104. https://doi.org/10.1016/j.agrformet.2014.08.003.

Han, M., Zhang, H., DeJonge, K.C., Comas, L.H., Gleason, S., 2018. Comparison of three crop water stress index models with sap flow measurements in maize. Agric. Water Manag. 203, 366–375. https://doi.org/10.1016/j.agwat.2018.02.030.

Hartmann, H.D., Pfülb, E., Zengerle, K.H. (2000): Wasserverbrauch und Bewässerung von Gemüse. Geisenheimer Berichte der Forschungsanstalt Geisenheim, Band 44, 194 p.

Heinemann, S., Siegmann, B., Thonfeld, F., Muro, J., Jedmowski, C., Kemna, A., Kraska, T., Muller, O., Schultz, J., Udelhoven, T., Wilke, N., Rascher, U., 2020. Land surface temperature retrieval for agricultural areas using a novel UAV platform equipped with a thermal infrared and multispectral sensor. Remote Sens. 12, 1075. https://doi.org/10.3390/rs12071075.

Hoffmann, H., Jensen, R., Thomsen, A., Nieto, H., Rasmussen, J., Friborg, T., 2016. Crop water stress maps for an entire growing season from visible and thermal UAV imagery. Biogeosciences 13, 6545–6563. https://doi.org/10.5194/bg-13-6545-2016.

Horst, G.L., O'Toole, J.C., Faver, K.L., 1989. Seasonal and species variation in baseline functions for determining crop water stress indices in turfgrass. Crop Sci. 29, 1227–1232. https://doi.org/10.2135/cropsci1989.0011183×002900050028x.

Idso, S.B., Jackson, R.D., Pinter, P.J., Reginato, R.J., Hatfield, J.L., 1981. Normalizing the stress-degree-day parameter for environmental variability. Agric. Meteorol. 24, 45–55. https://doi.org/10.1016/0002-1571(81)90032-7.

Inoue, Y., Kimball, B.A., Jackson, R.D., Pinter, P.J., Reginato, R.J., 1990. Remote estimation of leaf transpiration rate and stomatal resistance based on infrared thermometry. Agric. . Meteorol. 51, 21–33. https://doi.org/10.1016/0168-1923(90)90039-9.

Irmak, S., Haman, D.Z., Bastug, R., 2000. Determination of crop water stress index for irrigation timing and yield estimation of corn. Agron. J. 92, 1221–1227. https://doi.org/10.2134/AGRONJ2000.9261221X.

Jackson, R.D., Idso, S.B., Reginato, R.J., Pinter, P.J., 1981. Canopy temperature as a crop water stress indicator. Water Resour. Res. 17, 1133–1138. https://doi.org/10.1029/WR017i004p01133.

Jackson, R.D., Kustas, W.P., Choudhury, B.J., 1988. A re-examination of the crop water stress index. Irrig. Sci. 9, 309–317. https://doi.org/10.1007/BF00296705.

Jones, H.G., 1999. Use of infrared thermometry for estimation of stomatal conductance as a possible aid to irrigation scheduling. Agric. Meteorol. 95, 139–149. https://doi.org/10.1016/S0168-1923(99)00030-1.

Jones, H.G., 1992. Plants and Microclimate — A Quantitative Approach to Environmental Plant Physiology, second ed. Cambridge University Press, Cambridge.

Jones, H.G., Vaughan, R.A., 2010. Remote Sensing of Vegetation: Principles, Techniques, and Applications. Oxford University Press, Oxford, New York.

Liu, N., Deng, Z., Wang, H., Luo, Z., Gutiérrez-Jurado, H.A., He, X., Guan, H., 2020. Thermal remote sensing of plant water stress in natural ecosystems. Ecol. Manag. 476, 118433 https://doi.org/10.1016/j.foreco.2020.118433.

Maes, W.H., Steppe, K., 2012. Estimating evapotranspiration and drought stress with ground-based thermal remote sensing in agriculture: a review. J. Exp. Bot. 63, 4671–4712. https://doi.org/10.1093/JXB/ERS165.

Mallick, K., Trebs, I., Boegh, E., Giustarini, L., Schlerf, M., Drewry, D.T., Hoffmann, L., von Randow, C., Kruijt, B., Araùjo, A., Saleska, S., Ehleringer, J.R., Domingues, T.F., Ometto, J.P.H.B., Nobre, A.D., de Moraes, O.L.L., Hayek, M., Munger, J.W., Wofsy, S. C., 2016. Canopy-scale biophysical controls of transpiration and evaporation in the Amazon Basin. Hydrol. Earth Syst. Sci. 20, 4237–4264. https://doi.org/10.5194/hess-20-4237-2016.

Mallick, K., Wandera, L., Bhattarai, N., Hostache, R., Kleniewska, M., Chormanski, J., 2018. A critical evaluation on the role of aerodynamic and canopy–surface conductance parameterization in SEB and SVAT models for simulating evapotranspiration: a case study in the Upper Biebrza National Park Wetland in Poland, 2018, 10, 1753 Water 10, 1753. https://doi.org/10.3390/W10121753.

Meinardi, D., Schröder, J., Riedel, A., Röttcher, K., Kraft, M., Grocholl, J., Dittert, K., 2021. Sensorgestützte Beregnung von Kartoffeln: Entwicklung des Crop Water Stress Index für Nordostniedersachsen. https://doi.org/10.3220/WP1628164998000.

Meron, M., Sprintsin, M., Tsipris, J., Alchanatis, V., Cohen, Y., 2013. Foliage temperature extraction from thermal imagery for crop water stress determination. Precis. Agric. 14, 467–477. https://doi.org/10.1007/s11119-013-9310-0.

Möller, M., Alchanatis, V., Cohen, Y., Meron, M., Tsipris, J., Naor, A., Ostrovsky, V., Sprintsin, M., Cohen, S., 2006. Use of thermal and visible imagery for estimating crop water status of irrigated grapevine. J. Exp. Bot. 58, 827–838. https://doi.org/10.1093/jxb/erl115.

Osroosh, Y., Troy Peters, R., Campbell, C.S., Zhang, Q., 2015. Automatic irrigation scheduling of apple trees using theoretical crop water stress index with an innovative dynamic threshold. Comput. Electron. Agric. 118, 193–203. https://doi.org/10.1016/J.COMPAG.2015.09.006.

Padhi, J., Misra, R.K., Payero, J.O., 2012. Estimation of soil water deficit in an irrigated cotton field with infrared thermography. Field Crop. Res. 126, 45–55. https://doi.org/10.1016/j.fcr.2011.09.015.

Paul, G., Gowda, P.H., Vara Prasad, P.V., Howell, T.A., Aiken, R.M., Neale, C.M.U., 2014. Investigating the influence of roughness length for heat transport (zoh) on the performance of SEBAL in semi-arid irrigated and dryland agricultural systems. J. Hydrol. 509, 231–244. https://doi.org/10.1016/J.JHYDROL.2013.11.040.

Rud, R., Cohen, Y., Alchanatis, V., Levi, A., Brikman, R., Shenderey, C., Heuer, B., Markovitch, T., Dar, Z., Rosen, C., Mulla, D., Nigon, T., 2014. Crop water stress index derived from multi-year ground and aerial thermal images as an indicator of potato water status. Precis. Agric. 15, 273–289. https://doi.org/10.1007/s11119-014-9351-z.

Santanello, J.A., Friedl, M.A., 2003. Diurnal covariation in soil heat flux and net radiation. J. Appl. Meteorol. 42, 851–862. https://doi.org/10.1175/1520-0450(2003)042<0851:DCISHF>2.0.CO;2.

Song, B., Park, K., 2020. Verification of accuracy of unmanned aerial vehicle (UAV) land surface temperature images using in-situ data. Remote Sens. 12, 288. https://doi.org/10.3390/rs12020288.

Stockle, C.O., Dugas, W.A., 1992. Evaluating canopy temperature-based indices for irrigation scheduling. Irrig. Sci. 13, 31–37. https://doi.org/10.1007/BF00190242.

Taghvaeian, S., Chávez, J., Hansen, N., 2012. Infrared thermometry to estimate crop water stress index and water use of irrigated maize in Northeastern Colorado. Remote Sens. 4, 3619–3637. https://doi.org/10.3390/rs4113619.

Taghvaeian, S., Chávez, J.L., Bausch, W.C., DeJonge, K.C., Trout, T.J., 2014. Minimizing instrumentation requirement for estimating crop water stress index and transpiration of maize. Irrig. Sci. 32, 53–65. https://doi.org/10.1007/s00271-013-0415-z.

Wang, X., Yang, W., Wheaton, A., Cooley, N., Moran, B., 2010. Automated canopy temperature estimation via infrared thermography: a first step towards automated plant water stress monitoring. Comput. Electron. Agric. 73, 74–83. https://doi.org/10.1016/J.COMPAG.2010.04.007.

Wessolek, G., Kaupenjohann, M., Renger, M., 2009. Bodenphysikalische Kennwerte und Berechnungsverfahren für die Praxis. Technische Universität Berlin, Selbstverlag.

Zhang, L., Niu, Y., Zhang, H., Han, W., Li, G., Tang, J., Peng, X., 2019. Maize canopy temperature extracted from UAV thermal and RGB imagery and its application in water stress monitoring. Front. Plant Sci. 10, 1270. https://doi.org/10.3389/FPLS.2019.01270/BIBTEX.